

Contents lists available at ScienceDirect

Journal of Volcanology and Geothermal Research

journal homepage: www.journals.elsevier.com/journal-of-volcanology-and-geothermal-research





Unravelling the dynamics and hazards of the June 3rd, 2018, pyroclastic density currents at Fuego volcano (Guatemala)

Sylvain J. Charbonnier ^{a,*}, Franco Garin ^a, Lizzette A. Rodríguez ^b, Karla Ayala ^b, Sahira Cancel ^c, Rudiger Escobar-Wolf ^d, Gustavo Chigna ^e, Carla Chun-Quinillo ^f, Dulce González ^f, William Chigna ^g, Kevin Chun-Quinillo ^e, Roberto Mérida ^e, Francisco Juarez ^h, Eliza S. Calder ⁱ

- ^a School of Geosciences, University of South Florida, United States
- ^b University of Puerto Rico Mayagüez Campus, PO Box 9000, Mayagüez, 00681, Puerto Rico
- ^c Michigan State University, United States
- ^d Michigan Technological University, United States
- ^e Instituto Nacional de Sismología, Vulcanología, Meteorología e Hidrología (INSIVUMEH), Edificio Central, 7a Avenida 14-57, zona 13, Ciudad de Guatemala, Guatemala
- ^f Universidad Mariano Gálvez, Guatemala
- g Unidad de Volcans, Coordinadora Nacional para la Reducción de Desastres (CONRED), Avenida Hincapié 21-72, zone 13, Ciuda de Guatemala, Guatemala
- ^h Ministerio de Energia y Minas, 24 calle 21-12, zona 12, Ciudad de Guatemala, Guatemala
- i School of GeoSciences, University of Edinburgh, UK

ARTICLE INFO

Keywords: Pyroclastic density currents Fuego volcano Hazards Flow dynamics Conceptual model

ABSTRACT

The June 3rd, 2018, eruption of Fuego volcano (Guatemala) produced a complex sequence of small-volume pyroclastic density currents (PDCs) that inundated all sectors around the volcano and propagated >12 km on the southeastern flank, deposited ~50 million m³ of pyroclastic material, and killed at least 430 people in the village of San Miguel de Los Lotes and along the RN-14 road. This eruption has illustrated once again that the behavior of small-volume PDCs remains difficult to predict, demonstrating the need for an improved physical understanding of their generation, transport and depositional processes to ultimately improve assessment of their local hazard potential. In this work, we present preliminary results of an interdisciplinary study of the 2018 PDC deposits of Fuego, integrating: (1) field data of the pristine deposit characteristics recorded immediately after the eruption and after one rainy season, (2) sedimentological data (including grain size distributions and componentry) from samples collected at each lobe front and several exposed stratigraphic sections inside three principal ravines draining the volcano and affected by the eruption (Seca, Ceniza and Las Lajas), (3) preliminary quantification of the observed range of different clast surface textures, shape and vesicularities, as determined by SEM analyses, (4) surface morphological data from high-resolution satellite and aerial photography, and (5) advanced digital terrain model analysis correlated with sedimentological data to reconstruct the sequence of events on June 3rd and propose a conceptual model of PDC generation and emplacement on the SE flank of Fuego. In this model, a sequence of packages of material involved in discrete failure events of a perched mass of pyroclastic material accumulated within an old collapse structure on the upper SE flank, corresponds to the emplacement of a series of pulses of valley-confined PDCs down the Las Lajas channel. Headwall failures and gravitational collapses correlate with specific stratigraphic, sedimentological and textural characteristics of the valley-confined PDC units. The duration of individual granular collapse events serves as a proxy for the mobility of the triggered series of PDCs. Also, our detailed stratigraphic work shows evidence of stacked, massive flow units deposited by rapid stepwise aggradation of successive block-and-ash flow (BAF) pulses and their distribution along the southeastern flank supports the interpretation that the June 3rd PDCs, including the dilute parts of the currents, were largely controlled by the topography. The lack of strong changes in the grain size distributions of the fine sub-populations inside the seven valley-confined BAF lobate front units, together with their high content of fines, imply the presence of a self-limiting attrition process, decreasing the bulk porosity of such long-runout BAFs and lowering their effective friction coefficient during transport to reach longer runout distances. This multi-faceted approach completes previous studies already performed on small-volume PDCs at other volcanoes

^{*} Corresponding author.

E-mail address: sylvain@usf.edu (S.J. Charbonnier).

1. Introduction

On June 3rd, 2018, an eruption of Fuego volcano in Guatemala generated pyroclastic density currents (PDCs) that inundated the village of San Miguel de Los Lotes and reached 12 km from the summit, killing several hundred people. This eruption has illustrated once again that the behavior of small-volume PDCs remains difficult to predict, demonstrating the need for an improved physical understanding of their generation, transport, and depositional processes to ultimately improve assessment of their local hazard potential. In this work, we present the results of an multi-faceted study of the 2018 PDC deposits, integrating: (1) field data of the pristine deposit characteristics recorded in the months after the eruption and after the deposits had been dissected by one rainy season, (2) sedimentological data (including grain size distributions and componentry) from samples collected at each deposit lobe front and several exposed stratigraphic sections inside three main barrancas (the term corresponds to 'ravines') affected by the eruption (Seca, Ceniza and Las Lajas), (3) preliminary quantification of the observed range of different clast surface textures, shape and vesicularities, as determined by SEM analyses, (4) surface morphological data from high-resolution satellite and aerial photography, and (5) advanced digital terrain model analysis correlated with sedimentological data to reconstruct the sequence of events on June 3rd and propose a conceptual model of PDC generation and emplacement on the SE flank of Fuego.

1.1. Small-volume pyroclastic density currents (PDCs) and their overspill hazards

Small-volume (usually $<10^7 m^3$) pyroclastic density currents (PDCs) are complex and dangerous volcanic mass flows, composed of a hot mixture of gases and particles (Lube et al., 2020) and often generated from gravitational lava dome or small column collapses. They can flow over distances typically longer than 3 km and at speeds up to 100 km/h (Brown and Andrews, 2015). Our study focuses on concentrated PDCs, which are two-layer currents composed of a concentrated basal layer (more than \sim 40–60 vol% of particles) and an overriding dilute upper layer (<1 vol% of particles), also called the ash-cloud surge. There are no field observations supporting dilute PDCs exhibiting a dilute layer with a bedload region (Andrews, 2014; Brosch and Lube, 2020; Valentine, 2020) to be relevant here.

The basal part of small-volume, concentrated PDCs tends to be channelized in deep and narrow valleys of volcanoes. Previous studies have demonstrated that channelization can enhance flow runout by confining the entire mass over a restricted area, preventing rapid lateral spreading and efficient energy dissipation (Andrews and Manga, 2012; Calder et al., 1999; Charbonnier et al., 2013; Jessop et al., 2012; Ogburn et al., 2014; Woods et al., 1998). The interaction between topography and PDCs has been studied for decades (e.g., Branney and Kokelaar, 2002; Druitt, 1998; Kubo Hutchison and Dufek, 2021; Valentine, 1987). However, studies have mostly focused on dilute PDCs (Andrews, 2014; Andrews and Manga, 2011; Bursik and Woods, 1996; Doronzo et al., 2010; Woods et al., 1998) rather than concentrated ones. Interestingly, concentrated PDC overspill events usually occur when the flow encounters a sudden topographical change (Lube et al., 2011; Gertisser et al., 2012; Charbonnier et al., 2013; Macorps et al., 2018). Even though small-volume PDCs are channelized in valleys of volcanic edifices, most of fatalities are due to the unpredicted overspill of the flows from the channel confines and a rapid inundation of the interfluves, as the overspill can travel up to a few kilometers from its overflow point (i. e., Merapi 2006 and 2010, Charbonnier and Gertisser, 2011; Charbonnier et al., 2013).

As detailed recently in Gueugneau et al. (2021), Kubo Hutchison and Dufek (2021), and Lerner et al. (2022), PDC overspills exhibit various depositional and dynamical characteristics, and here we distinguish two different types: 1) 'PDC overspill', when the concentrated basal layer of a PDC escapes the valley at a specific location, usually, but not always, accompanied by its upper ash-cloud surge. If this overspill continues to flow along valley banks, volcanoclastic terraces and interfluves, it is usually named 'overbank flow' to distinguish it from its parent 'valleyconfined flow'; 2) 'ash-cloud surge detachment', when only the dilute ash-cloud surge decouples from the concentrated basal layer and escapes the confining valley to propagate on its own. Several studies suggest that PDCs properties (volume, flow rate) and the relative scale and geometry of the valley are key parameters controlling overspills (Lube et al., 2011; Gertisser et al., 2012; Charbonnier et al., 2013; Ogburn et al., 2014; Macorps et al., 2018; Gueugneau et al., 2021; Kubo Hutchison and Dufek, 2021; Lerner et al., 2022). A deeper understanding of the interaction between the valley-confined flow and the topography, as well as the evolution of the internal flow conditions during emplacement, is needed to better characterize the mechanisms of PDC overspills and better assess related hazards.

1.2. Fuego volcano and the 2018 eruption

Fuego volcano (3763 m a.s.l.) is the southernmost and currently most active stratocone of the Fuego-Acatenango volcanic complex in Guatemala, located $\sim\!40$ km southwest of the capital, Guatemala City. With over 50 eruptions with Volcanic Explosivity Index (VEI) ≥ 2 recorded since 1524, Fuego is one of the most active volcanoes in Central America (Global Volcanism Program, 2022), with a history of producing both violent Strombolian to Vulcanian (Berlo et al., 2012; Waite et al., 2013) and sub-Plinian eruptions (Escobar Wolf, 2013; Rose et al., 2008). In 1999, after two decades of quiescence, Fuego entered a new period of persistent eruptive activity that continues until the present day. This activity is characterized by a persistent background of Strombolian/Vulcanian ash-rich explosions (Patrick et al., 2007), which are interspersed with discrete events of larger energy and violence, referred as "paroxysms" (Lyons et al., 2010; Martin and Rose Jr., 1981).

The June 3rd, 2018, paroxysmal eruptive cycle began with an increase of seismicity at 3.00 am local time, quickly followed by strong summit explosions at 6.00 am, with loud rumbling and shockwaves felt by the population (INSIVUMEH, 2018c). The intensity increased during the morning and according to monitoring data acquired by INSIVUMEH (Instituto Nacional de Sismología, Vulcanología, Meteorología e Hidrología) during the eruption, as well as eyewitness accounts and detailed reports, the first series of PDCs on that day occurred at 10.00 am and descended the Seca, Santa Teresa, and Ceniza barrancas (INSIVU-MEH, 2018c) (Fig. 1). The explosivity became sustained between 11.30 am and 1.30 pm and peaked at 1.10 pm at which point a 16-19 km-high sub-Plinian eruption column had formed (Pardini et al., 2019) and associated tephra fallout dispersion up to ~40 km downwind toward the NW-NE sector from the volcano. During the peak of the sub-Plinian phase, PDCs were seen traveling down toward La Reunion golf resort in the barranca Las Lajas (Fig. 1). It was only shortly after 2.20 pm, about one hour after the size of the eruption plume decreased significantly, that the first PDC reached the bridge of the RN-14 road that crosses the eastern Las Lajas channel (Figs. 1 and 2). The peak of PDC activity occurred between 3.00 pm and 3.30 pm, where three PDC pulses can be observed from photographs and video footage taken by photographer Jiuwit Rosas (and shared by CONRED) along the RD-14 road (Fig. 2). The timing of these three PDC pulses was correlated with three periods of increased seismic activity recorded by INSIVUMEH

at the FG8 seismic station (located in Panimache, see Fig. 1) between 3.00 pm and 3.30 pm (Fig. 2A). The first PDC pulse occurred at 3:05 p.m. and at exactly 3.09 pm, it impacted the Las Lajas bridge before overflowing into the RN-14 road. A photograph (Fig. 2B) taken at the bridge just before 3.09 pm shows the front of the PDC pulse arriving in the background, as well as the upstream portion of the eastern Las Lajas channel already partially filled with PDC deposits from an earlier flow, probably shortly after 2.20 pm. A few seconds later, this first PDC pulse overspilled the bridge to inundate the RN-14 road (Fig. 2C). According to the video footage, between 3:09 p.m. and 3:12 p.m., another PDC pulse arrived at the bridge and overflowed the highway, passing Finca La Flor and continuing to flow along the RN-14 road (following the local slope) in direction of San Miguel de Los Lotes (Fig. 2D). From 3:12 pm to 3:16 pm, a third PDC pulse was recorded by the seismic station and captured a few minutes later by photographs taken at 3.18 pm from the entrance of El Rodeo village along the RN-14 road, that show a PDC overflowing in the direction of San Miguel de Los Lotes (Fig. 2E). According to reports from CONRED, several PDC pulses descended in this direction a few minutes later (fourth seismic pulse in Fig. 2A?) and led to the total inundation, destruction, and burial of two-thirds of the northwestern part of the village of San Miguel de Los Lotes. After 3.30 pm, PDC activity waned, ceasing altogether shortly after 4.30 pm. Official numbers report 430 people missing, although the death toll as reported by survivors from Los Lotes might be as high as 2000 (Naismith et al., 2019). There is broad consensus that the official death toll is underestimated. The eruptive cycle ended after $\sim\!16$ h, when activity was reduced to an ash column of $\sim\!4500$ m a.s.l (INSIVUMEH, 2018d), with weak to moderate explosions at the summit.

In the days following the eruption, the activity level remained high, with multiple PDCs recorded on June 5th, 7th, 8th, and 12th, mostly descending the east flanks (INSIVUMEH, 2018a, 2018b, 2018e, 2018f). The month of June falls in the rainy season, and intense rains in the afternoons are typical. The frequent and intense periods of rainfall occurring immediately after June 3rd produced many moderate- to high-volume lahar events in the barrancas of Las Lajas, Honda and Seca (INSIVUMEH, 2018g). The volume of the June 2018 PDC deposits in Las Lajas has been estimated between 15x10⁶m³ to 30x10⁶m³ using field estimates and satellite imagery (Albino et al., 2020; Ferres and Escobar Wolf, 2018; Naismith et al., 2019).

2. The June 3rd, 2018, PDC deposits

2.1. Field data collection and methodology

The June 3rd, 2018, PDC deposits were investigated in the field during two field campaigns carried out in August 2018 and January 2019. Due to the widespread distribution of the 2018 deposits, which inundated several barrancas around the volcano, we focused our field data collection on the sector most affected by the PDC activity, on the southeastern flank of the volcano along the barranca of Las Lajas

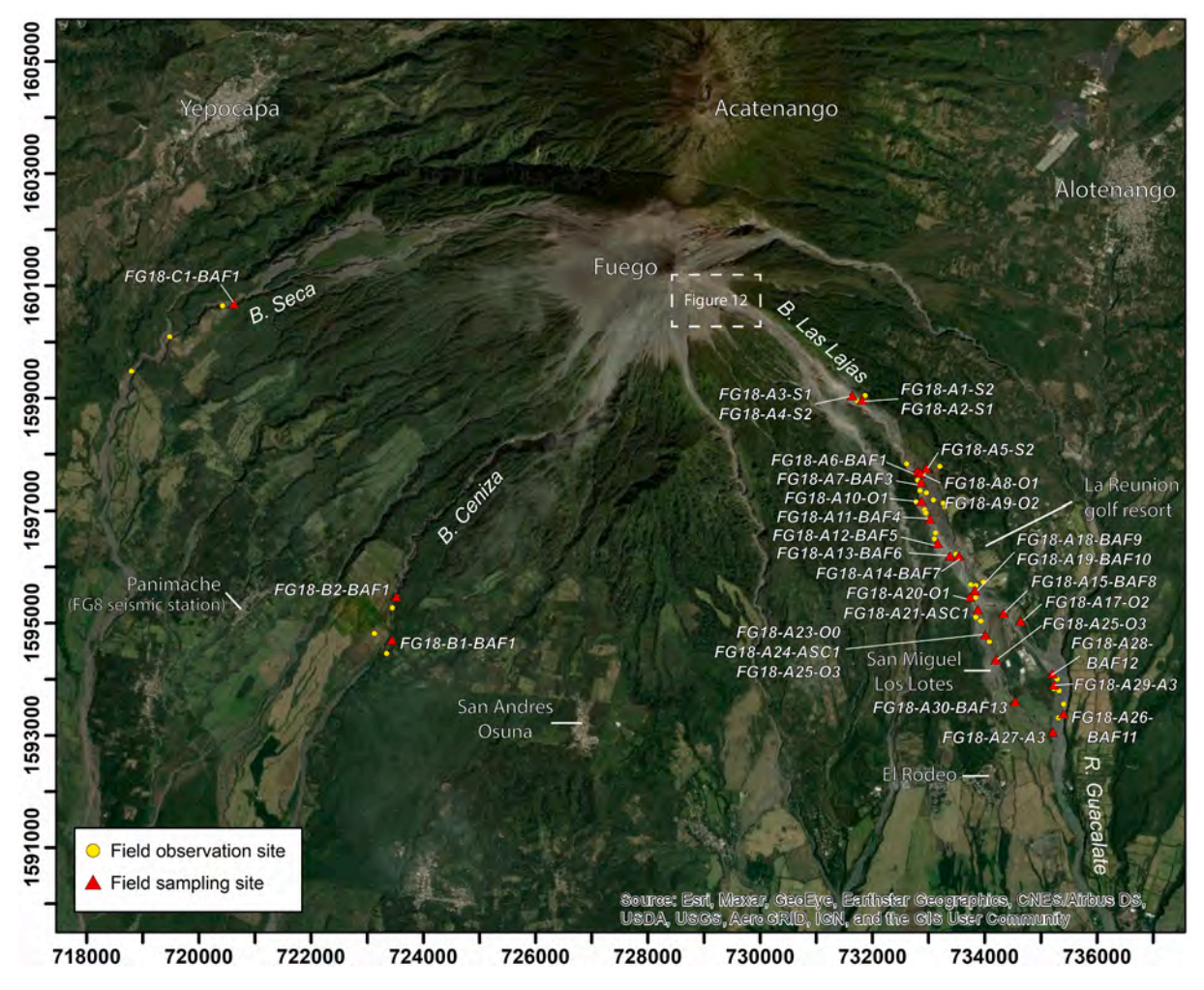


Fig. 1. Satellite image of Fuego volcano and its surrounding (source: ESRI) including the main volcanoes and villages (in white), as well as the primary channels affected by the 2018 eruption ('Barrancas', B. and 'Rio', R., in italic). Sampling sites and sample names for sedimentological analyses, as well as locations of field measurements are also included. White dashed box indicates the extent of Fig. 12.

(Fig. 1). PDC deposit samples were also collected in two other barrancas located in the southern and western flanks, Ceniza and Seca, but the availability of fresh PDC outcrops in these valleys that was not affected by reworking by the post-eruptive lahars was already limited at the time of sampling. Moreover, our interest was focused on the valley-confined and overbank lithofacies of the PDC deposits, while field analyses of the widespread, cm- to dm-thick proximal (< 4 km from the summit) surge deposits were restricted to the few accessible outcrops located in this area (Fig. 1). Deposit outlines were mapped in the field using a combination of handheld GPS, digital cameras, drone surveys and portable GIS software on tablets. Thickness measurements of the different PDC units were collected using a TruePulse 360 laser rangefinder with a vertical accuracy of <0.3 m within the range of horizontal distances (<100 m) measured. Additional thickness measurements were collected digitally, using the new elevation data acquired from a 1 m DEM (from Aerobots, Inc.) generated <24 h after the PDCs were emplaced. Stratigraphic logs were built at twenty-six locations to identify and describe the different PDC units and their facies, as well as tentatively correlate them longitudinally within the same drainage system.

A total of thirty-four samples were collected for sedimentological analysis to assess PDC units and their corresponding facies – as defined as part of the stratigraphic survey. This sedimentological analysis focused on (1) grain size distribution and (2) componentry with the aim

of differentiating the different PDC units based on the particle size and lithological characteristics, respectively. A tephra fallout sample collected by a resident the day of the eruption at San Miguel Dueñas (located ~10 km NE of the summit) and corresponding to fallout deposits from the sub-Plinian phase that occurred between 11.30 am and 1.30 pm on June 3rd was added to the analyses for comparison. Samples analyzed for grain size distribution were individually weighed and sieved at 1 phi intervals - wet sieving was selected as the preferred approach to avoid particle comminution. The selected range of particle sizes for wet sieving was set from -4 phi (32 mm) down to +5 phi (32 μm). After the wet sieving process completion, each sample's individual grain size fractions were dried in an oven for 24 h and then each fraction weighed independently. Loss of fine particle estimates <5 phi during the wet sieving process was calculated and found to never exceed 10 wt% of the total sample mass for valley-confined and overbank deposits (and < 25 wt% for ash-cloud surge and fallout deposits). A total of thirty samples were selected for further analysis using the GRADISTAT software (Blott and Pye, 2001) to compute statistical parameters of the grain size distributions. Those samples presenting a polymodal distribution were further analyzed using the DECOLOG software (www. DE COLOG.org; Borselli and Sarocchi, 2009) to apply deconvolution to polymodal size distributions, primarily with the goal of distinguishing between fine and coarse particle sub-populations. The deconvolution

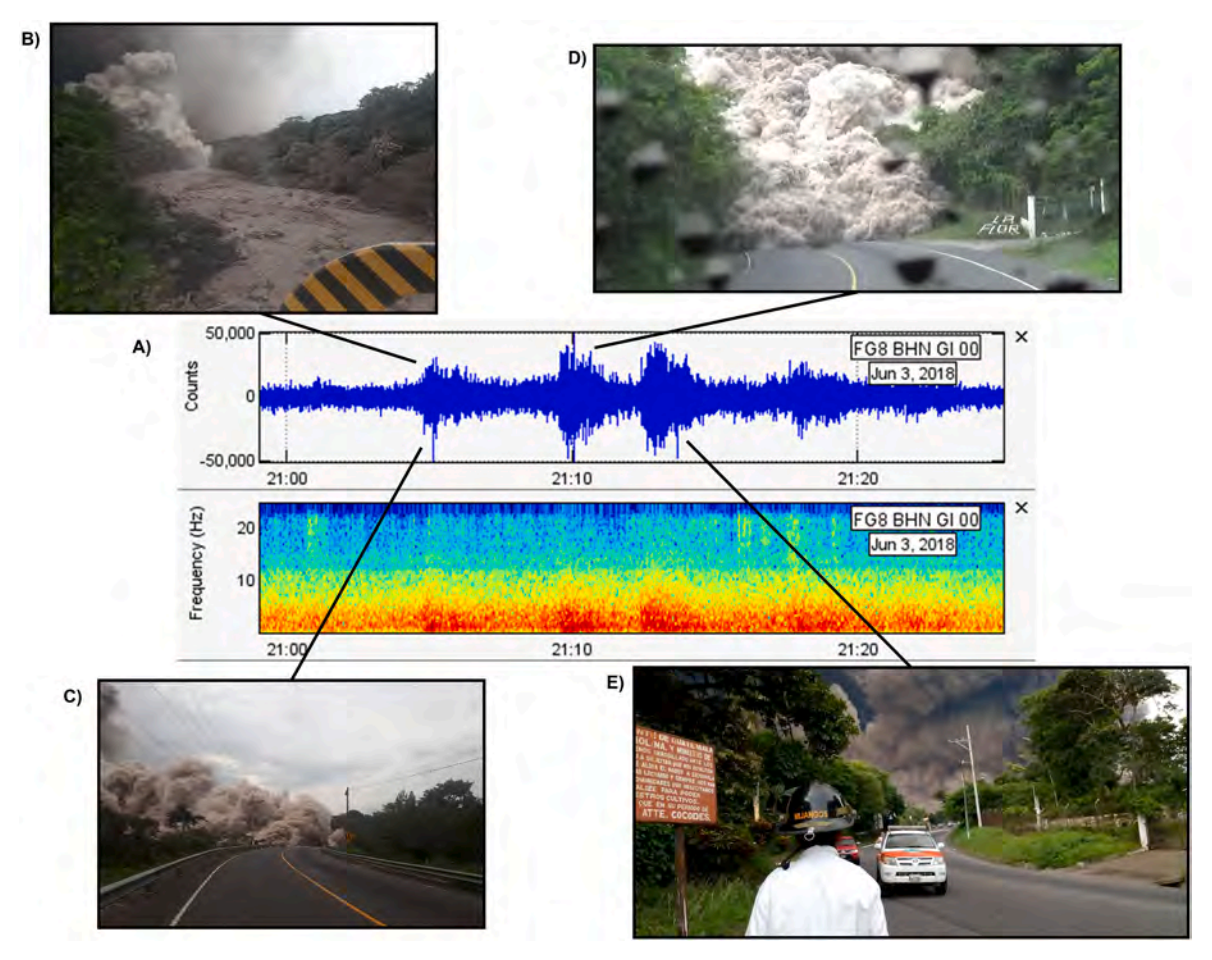


Fig. 2. Sequence of events associated with the peak of PDC activity between 3.00 pm and 3.30 pm on June 3rd, 2018. A) Seismogram obtained from the INSIVUMEH seismic station FG8 located in OVFGO at Panimache (see Fig. 1 for location) showing the seismic counts (upper graph) and frequencies (lower graph) associated with the PDC activity between 3.00 and 3.30 pm on June 3rd. Time is in UTC. B) Photograph taken at the bridge just before 3.09 pm shows the front of the PDC pulse arriving in the background, as well as the upstream portion of the eastern Las Lajas channel already partially filled with PDC deposits from an earlier flow, probably shortly after 2.20 pm. C) A few seconds later, this first PDC pulse overspilled the bridge to inundate the RN-14 road. D) Between 3:09 p.m. and 3:12 p.m., another PDC pulse arrived at the bridge and overflowed the highway, passing Finca La Flor and continuing to flow along the RN-14 road in direction of San Miguel de Los Lotes. E) From 3:12 pm to 3:16 pm, a third PDC pulse was captured by photographs taken at 3.18 pm from the entrance of El Rodeo village along the RN-14 road (see Fig. 1 for location), showing a PDC overflowing in the direction of San Miguel de Los Lotes.

process consists of dividing a polymodal distribution into a mixture of lognormal distributions based on peak components that are the most statistically representative of the different particle size sub-populations.

In addition to the grain size distribution analyses, sixteen samples were selected for lithological component analysis using a binocular optical microscope. This process involves handpicking a randomized set of n clasts (here n is between 700 and 1600) and performing point counting of individual particles into visually discernable groups based on colors, contents, and shapes. The 1 phi grainsize fraction was chosen

because 1) it presents the largest weight values, and thus the most abundant matrix grain size fraction in most of our samples, and 2) the size range of this fraction ($500 \mu m$ to $1000 \mu m$) prevents particle clustering (i.e., glass adhering to and/or crystals attached to other grains) while being not too tedious to work with under the binocular. Particles were assigned to one of eleven recognized lithological component categories: (a) brown glass, (b) dense black glass, (c) vesiculated black glass, (d) other colored glass, (e) black scoria, (f) brown scoria, (g) dense grey clasts, (h) free crystals, (i) oxidized clasts, (j) partially oxidized

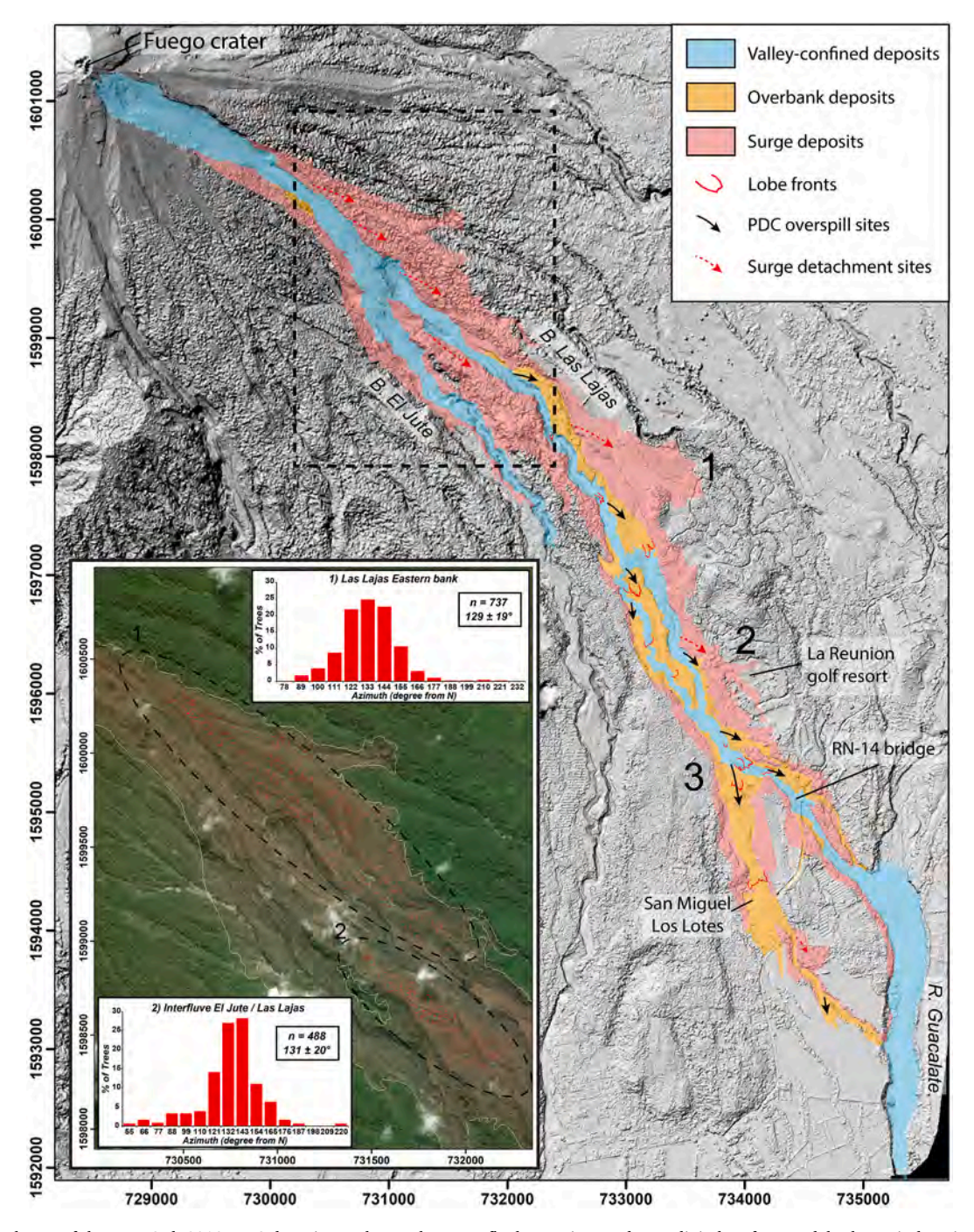


Fig. 3. Geological map of the June 3rd, 2018, PDC deposits on the southeastern flank superimposed on a digital surface model. The main locations of interest and primary channels are also included. Black numbers 1, 2 and 3 indicate the three main PDC overspill sites discussed in the text. Inset: Map of the azimuth ($^{\circ}$ from North) of trees (red lines) downed and transported by the June 3rd, 2018, PDCs at two locations along the proximal Las Lajas barranca (black dashed ellipsoids outline the two locations) superimposed on a Worldview satellite image acquired in June 2018 after the eruption (source: Digital Globe). Panels 1) and 2) show histograms of the distribution ($^{\circ}$ 0) of tree azimuths ($^{\circ}$ 1 = number of trees) for 11 $^{\circ}$ 2 bins for each of the regions. (For interpretation of the references to color in this figure legend, the reader is referred to the web version of this article.)

clasts, and (k) hydrothermally altered clasts, and then further analyzed with a scanning electron microscope (SEM) to further investigate their surface textures.

2.2. Mapping and surface characteristics

Based on the combination of detailed analyses of various highresolution optical images and field-based surveys performed just after the eruption, a detailed deposit map of the June 3rd, 2018, PDC deposits is presented in Fig. 3. The PDC deposits comprise: (1) valley-confined PDC deposits in the Las Lajas, El Jute, Ceniza and Santa Teresa/Seca barrancas; (2) overbank PDC deposits, where parts of the channeled PDCs spread laterally onto interfluves at several sites (black arrows on Fig. 3) along the main channels and were subsequently re-channeled into the surrounding river valleys and adjacent tributaries; and (3) thin (\sim 0.5-m-thick) ash-cloud surge deposits that inundated large areas on the medial to proximal flanks, especially along seven of the principal barrancas draining the volcano. A singe zone is also recognized along valley margins and/or in marginal vegetated/forested areas affected by valley-confined and overbank PDCs. Using the 'Geometric Attributes' tool in ArcGIS, the azimuth (degrees from North) of downed trees (n \sim 1225) in the two main proximal areas affected by the ash cloud surge on June 3rd were derived from satellite imagery and used to infer the main current directions (inset in Fig. 3).

The surface of the valley-confined deposits shows a chaotic morphology with contrasted dark, convex boulder-rich ridges, and light-colored margins of finer grained material. They are characterized by the presence of several overlapping lobate deposits (we outlined 13 of them on Fig. 3) with steep, bouldery and clast-supported fronts, similar to those reported at Merapi (Charbonnier and Gertisser, 2008;



Fig. 4. Impacts of the June 3rd, 2018, PDCs on the southeastern flank of Fuego as captured during the August 2018 field campaign. Red arrows indicate the main flow direction. a) View of the southeastern flank of Fuego from the eastern bank of Las Lajas barranca. Dashed red line shows the extent of the ash-cloud surge. b) Overbank PDC lobate deposits over the La Reunion golf course. c) Overbank PDC deposits just a few meters downstream of overspill location 3 (Fig. 3) showing intense substrate erosion (foreground) and wedge-shaped deposits at the overspill site (background). d) Moderately-sorted, ash-cloud surge deposits in the proximal, eastern bank of Las Lajas barranca, located about 4 km from the summit, with downed and broken trees on top. e) Ash-cloud surge deposits in the eastern bank of Las Lajas captured at the same distance as d) but closer to the main channel, showing intense substrate erosion and tree damages. The main valley-confined PDC deposits are present on the left-hand side of the picture. f) Thin, well-sorted ash-cloud surge deposits on the same interfluves as d) and e) but further away from the main channel, that only partially burned and/or snapped tree branches, coffee beans and/or soil. g) Strong erosional features on the western valley margins along the Las Lajas barranca caused by the 2018 PDCs (~4.5 km from summit), where the vegetation was completely removed and pre-existing substratum was scoured and striated, exposing older stratigraphy. The main valley-confined PDC deposits are present in the center of the picture, while the ash-cloud surge deposits are in the foreground. h) Heavily damaged concrete bathroom structure from the impact of the 2018 overbank PDCs at the western edge of La Reunion golf course (overspill site 2, Fig. 2). i) Friction mark ~10 cm long and ~ 3 cm wide on a lava flow block transported by the 2018 valley-confined PDC deposits in Las Lajas. j) Aluminum railing pulled out, transported, and wrapped around a scorched tree trunk by the 2018 overbank PDCs at La Reu

Schwarzkopf et al., 2005), Colima (Macorps et al., 2018; Saucedo et al., 2002), Unzen (Ui et al., 1999) and Soufriere Hills (Cole et al., 2002)... The surface of the overbank deposits is generally light colored and contrasts with the darker surface of the valley-confined deposits (Fig. 3). The overbank deposits produced thick, convex fans and lobes of poorly sorted material on the interfluves and volcanoclastic terraces at the margins and/or between the inundated channels. Based on both satellite image analyses and field observations, numerous large blocks, several meters in size, protrude well above the valley-confined deposit surface and the maximum clast size reaches a peak at some intermediate distance (up to 10 m diameter), decreasing toward the proximal reaches as well as to the distal part of the PDC deposits. Associated ash-cloud surge deposits extend beyond the limit of the overbank deposits in the proximal area and generated damage to trees as well as topsoil stripping in the nearby coffee plantations (Fig. 4a). Several stripes of singed trees are also clearly visible on the outer banks of the Las Lajas barranca. Gradual lateral deposit facies transition and their decreasing associated impacts on the surrounding landscape can be observed across a section of the proximal Las Lajas channel located ~4 km from the summit: 1) from the thick, poorly-sorted valley-confined deposits that completely filled the pre-eruptive channels; 2) to the thinner, moderately-sorted overbank deposits on valley margins that uprooted, burned trees in the direction of the flow, buried volcanoclastic terraces and stripped or scorched marginal vegetated areas; and finally 3) the thin, well-sorted ash-cloud surge deposits on the interfluves that only partially burned and/or snapped tree branches, coffee beans and/or soil (Fig. 4d-f).

Damages to vegetation, agriculture, buildings and infrastructure are related to the three main PDC overspill sites that occurred along the Las Lajas barranca (Fig. 3): 1) the first major PDC overspill occurred after a sharp bend in the valley at 5.5 km from the summit, with associated overbank and surge deposits that extended as far as ~1 km laterally away on the eastern side of the channel, impacting coffee plantations; 2) the second major PDC overspill (~700 m width) affected La Reunion Golf resort, located ~7.2 km from the summit, and was caused by channel constriction due to the presence of historical volcanoclastic terraces inside the eastern banks of Las Lajas where the Golf resort is built upon; 3) the third major PDC overspill occurred at a sharp bend of the Las Lajas barranca located 8.2 km from the summit, and led to the destruction and burial of two-thirds of the northwestern area of the village of San Miguel de Los Lotes by overbank PDCs, that propagated an additional 2.8 km downstream in an inactive western tributary of the Las Lajas barranca to reach the junction with the Guacalate river (Fig. 3). Overbank deposits in the village are up to ~5 m thick, and consist of massive, poorly sorted, with meters-sized boulders inside a medium-tofine ash matrix. The widespread destruction of most buildings in the northern part of the town along with a few surviving buildings of the same typology in the south and east parts suggests that destruction of buildings was caused by a combination of dynamic pressure and missile damage from large clasts carried by the PDCs (Lerner et al., 2022). The portion of the main road running along the south-east and east side of the town (RN-14) was completely inundated, and most of the damage (and many fatalities) occurred at the bridges crossing the western and eastern Las Lajas channels. Buildings and infrastructures of the Golf resort located on volcanoclastic terraces close to the Las Lajas channel were either highly damaged or destroyed (Fig. 4h, j). However, inside the golf resort, the energy of the overbank PDCs was low enough that they could be largely blocked by buildings and associated ash-cloud surges maintained similarly low velocities (< 5 m/s) and dynamic pressures (< 0.5 kPa), evidenced by their ability to fell only slim and very small (2-3 m height) trees or palms, but not to remove roof tiles or to move items located on tables inside buildings (Lerner et al., 2022). Other locations of minor PDC overspills (with lateral extension <200 m from the channel banks) found along the Las Lajas barranca are indicated on the map in Fig. 3.

In addition, some features were observed that affected both, large blocks within the deposits and blocks of pre-topographic substratum

along the valley walls exposed during emplacement of the successive PDCs. Randomly orientated friction or impact marks of various sizes up to ~ 10 cm long and ~ 3 cm wide were identified on all sides of large dense blocks within the deposits (Fig. 4i). Such marks were described previously from block-and-ash flow deposits at Merapi and Soufriere Hills volcano, Montserrat, where they were interpreted to be related to the high energy of block collisions, both with the pyroclastic-flow matrix trapped in between (Grunewald et al., 2000) or with each other (Schwarzkopf et al., 2001, 2002). Strong erosional features were observed at valley margins along the full flow length. At several locations along the Las Lajas barranca, the pre-existing substratum was scoured and striated (Fig. 4g), clasts were found embedded in tree trunks and tree barks were scorched or singed as high as 5 m above the surface of the PDC deposits, giving some indication of maximum current heights in these areas (Fig. 4k).

2.3. Main lithofacies and stratigraphy

The spatial imagery analysis and field investigations of the deposit surface revealed significant differences between deposits from valley-confined PDCs, overbank PDCs and ash-cloud surges. Based on the lithofacies scheme previously defined for the recent Merapi and Colima PDC deposits (Charbonnier et al., 2013; Charbonnier and Gertisser, 2011; Macorps et al., 2018), five main lithofacies are distinguished in this study to describe the internal architecture of the June 2018 PDC deposits in terms of the grain size, depositional features, structure, bedforms and matrix characteristics (coloration, grain-size, componentry): mBLA (Massive Blocks, Lapilli and Ash); mLA (Massive Lapilli and Ash); csLA (cross-stratified Lapilli and Ash); sLA (stratified Lapilli and Ash) and mA (Massive Ash). Fig. 5 depicts some of these lithofacies at selected locations along the June 2018 PDC deposits.

Stratigraphy of the June 2018 PDC deposits was limited by the availability of stratigraphic sections and amount of erosion that occurred inside the fresh deposits at the time of sampling. At most outcrops located inside the Las Lajas barranca, only the upper part of the June 2018 valley-confined deposits was exposed, and often restricted to the frontal overlapping lobes. Nevertheless, seventeen main depositional units have been identified along the Las Lajas channel, mainly based on their lithological and sedimentary characteristics, as well as longitudinal and lateral correlations of thin interbedded ash fall layers. Each stratigraphic unit represents either the emplacement of a different PDC or is associated with the deposition of a particular PDC layer (i.e., ash-cloud surge units csLA and sLA). A composite stratigraphic section of these units, along with their lithofacies description, are presented in Fig. 6.

2.3.1. Valley-confined facies

The presence of several overlapping lobate deposits with steep, bouldery and clast-supported fronts at the surface, as well as changes in the amount of oxidation and grain-size distribution of the matrix, were found to be the most reliable diagnostic features to identify valleyconfined unit boundaries. At the base of the vertical sequence, units mBLA1 and mBLA2 have a distinctive fine-grained, dark grey-to-brown matrix with only a small amount of oxidized and hydrothermally altered lapilli and blocks (Figs. 5 and 6). Matrix colors of the valley-confined units vary from grey to brown, with a gradual color change, as well as increases in matrix grain-size and abundance of oxidized lapilli and blocks (see next section), from unit mBLA1 to mBAL7 (Figs. 5 and 6). These changes can be correlated with an increase of iron oxidation in the matrix of PDC lobes that were emplaced toward the end of the PDC sequence on June 3rd afternoon. Grain fabric orientations are observed only in the upper units and stratigraphic sections from the proximal area (~4 km from the summit) with clast trains and long axes of elongated clasts (in the size range between -6 to -8 phi) mostly parallel to the flow direction. Coarse-tail grading is also observed in the same exposed units proximally, but is absent from all other sections downstream,

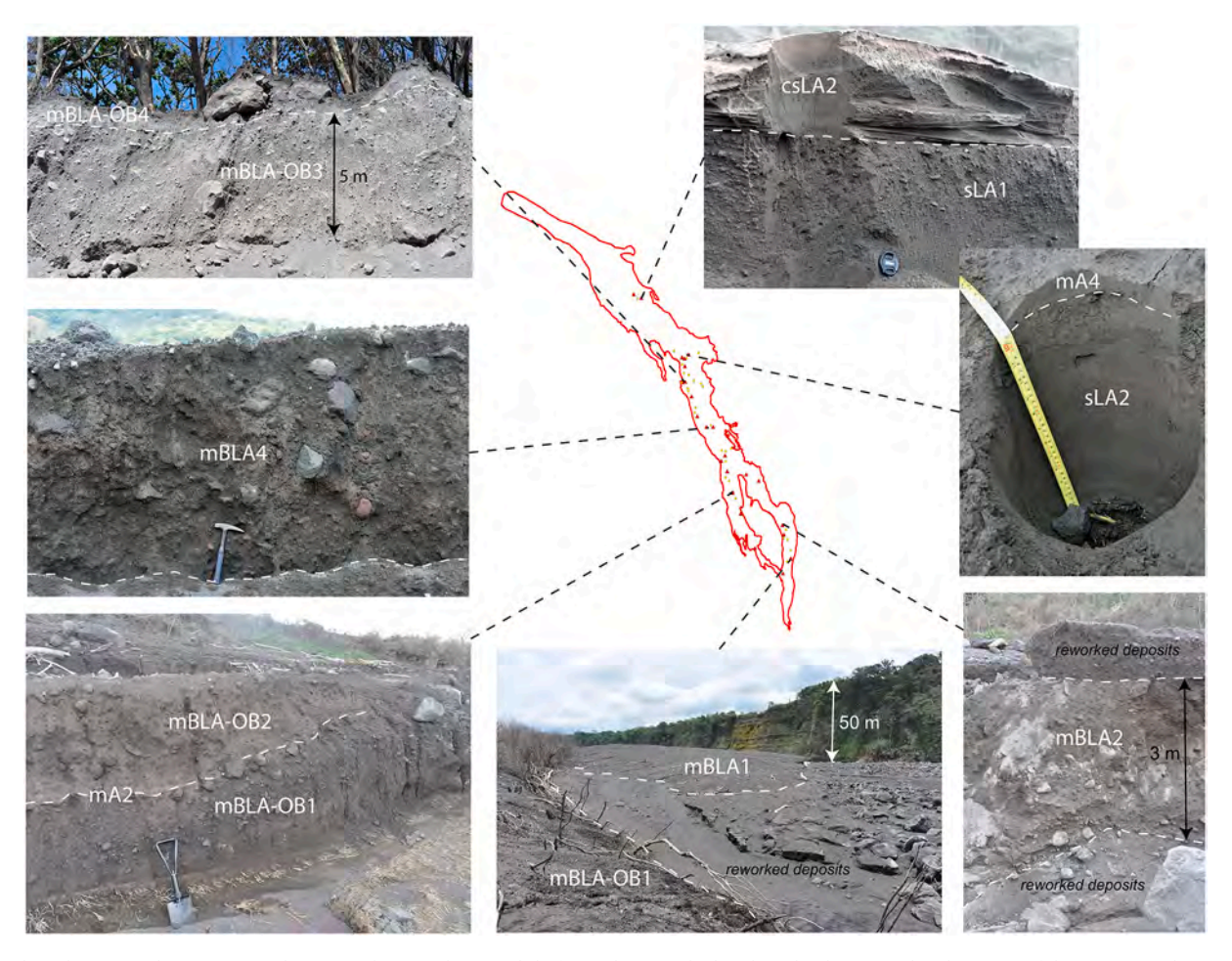


Fig. 5. Selected stratigraphic sections and pictures showing the main lithofacies distinguished to describe the internal architecture of the 2018 PDC deposits: mBLA (Massive Blocks, Lapilli and Ash); csLA (cross-stratified Lapilli and Ash); slA (stratified Lapilli and Ash); mA (Massive Ash). The term 'OB' indicates an overbank unit. Dashed white lines indicate depositional unit boundaries or interfaces between different facies.

where the most common facies is mBLA with random clast orientation and distribution. Thicknesses of exposed valley-confined units vary from 2 m to >20 m but are often between 3 and 7 m on average. The distribution of these channeled deposits inside the Las Lajas channel is not uniform, with as much as five stratigraphic units identified between 5.7 and 8.2 km from the summit (units mBLA3 to mBLA7 in Fig. 6), whereas only two valley-confined units (units mBLA1 and mBLA2) are observed in the distal area.

2.3.2. Unconfined facies

Two different types of unconfined deposits have been recognized from field investigations, namely overbank and ash-cloud surge deposits. As previously described for the 2006 and 2010 Merapi PDC deposits (Charbonnier et al., 2013; Charbonnier and Gertisser, 2011), two main types of overbank deposits, depending on the geometric conditions of overbanking and the morphology of the interfluve surface, are found in the 2018 Fuego PDC deposits: 1) wedge-shaped overbank deposits are mainly located close to the main channel (< 1 km laterally), with maximum thicknesses close to the valley walls and gradual lateral thinning toward the valley margins (i.e., PDC overspill sites 1 and 2 in Fig. 3); 2) re-channeled overbank deposits where overbank PDCs are rechanneled into first-order secondary tributaries on both sides of the main channel (i.e., PDC overspill site 3 in direction of San Miguel de Los Lotes). Within these tributaries, the re-channeled overbank deposits consist of poorly sorted mBLA or mLA deposit facies, either without grading or with weak apparent coarse-tail grading. In contrast to the first type of overbank deposits, their thicknesses (up to 2 m) remain remarkably constant along their runout length. As many as four overbank units (mBLA-OB1 to mBLA-OB4 in Fig. 6) have been identified in the stratigraphy, but only the two basal ones (mBLA-OB1 and m(B)LA-OB2) were found downstream of PDC overspill site 3. Unit mBLA-OB1 is the only overbank unit that reached San Miguel de Los Lotes and is correlated with the late arrival of the PDC overbank flow witnessed by the CONRED team along the RN-14 road around 3.18 pm (Fig. 2E), a few minutes after the passage of the two valley-confined PDCs at the Las Lajas bridge that reached the Guacalate river (units mBLA1 and mBLA2 in Figs. 5 and 6).

Two stratified to cross-stratified lapilli and ash units (sLA1 and csLA2 in Figs. 5 and 6) were found in the proximal sections at ~4 km from the summit, inside extensive ash-cloud surge deposits emplaced on top of marginal vegetated/forested terraces on the eastern side of Las Lajas barranca (Fig. 4). They consist of an alternation of lapilli clasts (often imbricated) inside a brownish to reddish matrix with finer grained, massive, greyish ash layers. Dune bedforms inside unit csLA2 do not exceed 50 cm in thickness and 1.5 m in length (Fig. 5). Closer to the Las Lajas active channel, the stratified surge basal unit sLA1 gradually becomes thicker (> 1 m), more poorly sorted and coarser grained (with blocks <20 cm) to reach the mBLA facies as an overbank deposit at lateral distances <50 m from the Las Lajas eastern wall (most proximal sampling site in Fig. 1). In the volcanoclastic terraces on the eastern side of Las Lajas at PDC overspill site 1 (Fig. 3), the topmost surge unit csLA2 grades into a ~ 30 cm-thick stratified lapilli and ash unit sLA2 which consists of ~10 sub-units with an alternation of fine- and coarse-grained ash (Fig. 5). A thin (< 3 cm) ash fallout layer (mA4 in Fig. 6) overlays

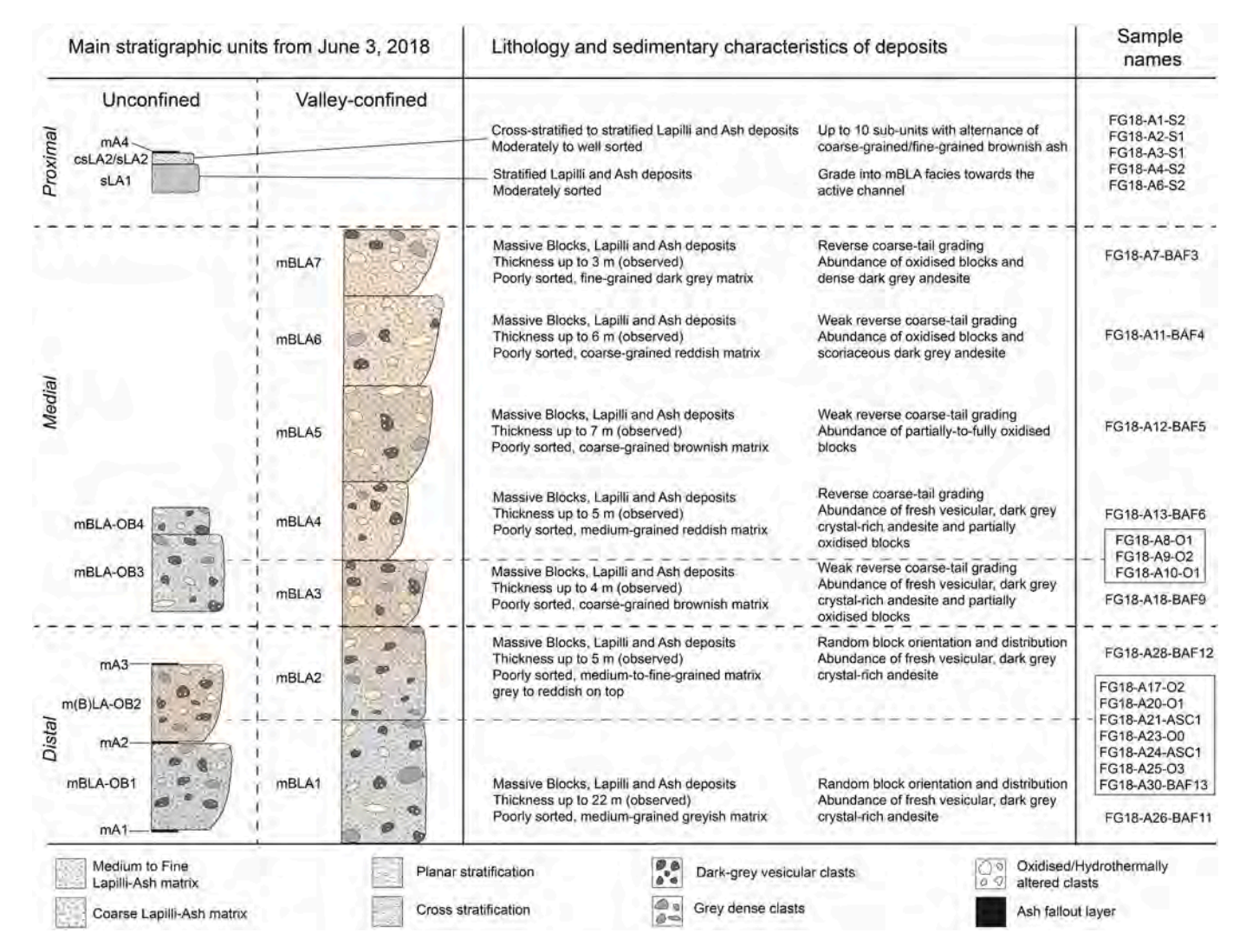


Fig. 6. Composite stratigraphic section (not to scale) of the main depositional units of the June 3rd, 2018, eruptive sequence along with their location, lithofacies description and corresponding sample names. Main lithological components and their relative abundances are also shown. See Fig. 1 for sample location.

this unit.

Just downstream of PDC overspill site 1 (Fig. 3) around \sim 6 km from the summit, two overbank units (mBLA-OB3 and mBLA-OB4) are visible on the western margin of the Las Lajas barranca. Unit mBLA-OB3 consists of a \sim 5 m-thick, poorly sorted deposit facies with a light grey matrix and > 1-m-diameter blocks while unit mBLA-OB4 is much thinner (<1 m thick) and finer grained (Figs. 5 and 6). A thin (<1 cm) layer of burnt vegetation is present between units mBLA-OB3 and mBLA-OB4. Overbank deposits with singed vegetation and snapped young trees are also visible on the eastern margin of the Guacalate river, at the frontal terminus of the June 2018 deposits (most distal sampling location in Fig. 1), where they consist of a \sim 1.5 m-thick, massive mBLA facies with weak reverse grading. A thin (<2 cm) ash fallout layer overlies the overbank deposits at that location (mA3 in Fig. 6).

Between 200 and 800 m downstream of PDC overspill site 3 in the western tributary of Las Lajas, an area of patchy deposition and stripped soil (Fig. 4c) corresponds to the emplacement of a \sim 70–90 cm-thick, massive, brownish lapilli and ash unit mLA-OB2 (Fig. 6) that locally overlies overbank unit mBLA-OB1 and grades downstream into the mBLA facies of overbank unit mBLA-OB2 (Fig. 5). The contact between m(B)LA-OB2 and mBLA-OB1 is either gradational or sharp with the presence of an interbedded, < 2 cm-thick ash fallout layer (mA2 in Figs. 5 and 6).

2.4. Matrix grain size distribution and componentry

The results of grain size analyses for the thirty samples collected is presented in Table 1, while the results obtained from deconvolution of the polymodal grain size distributions with DECOLOG are presented in Table 2. The vast majority of the valley-confined PDC samples analyzed present a bimodal distribution. GRADISTAT analyses using Derive Folk-Ward statistics for valley-confined samples (unimodal and bimodal) show that samples are mostly poorly sorted with sorting coefficients ranging from 2.6 to 3.0 phi and mean diameters of -0.4 and 0.3 phi (Table 1, Fig. 7a). The two modes (peak grain sizes) identified by the deconvolution process fall between $-4.2 \, \text{phi}$ and $-3.5 \, \text{phi}$ for the coarse sub-population, and between 0.6 and 1.9 phi for the fine sub-population (Table 2). Only one valley-confined sample presents a unimodal distribution with a mode of 0.5 phi. Samples collected from overbank PDC deposits also show mostly bimodal distributions with the two modes between -4.7 phi and -1.3 for the coarse sub-population, and 0.4 and 1.6 phi for the fine sub-population (Table 2). Most samples are fine skewed (where fine values are spread out), with the valley-confined and overbank samples being platykurtic whereas ash-cloud surge and fallout samples being mesokurtic with sorting coefficients ranging from 1.1 and 3.0 phi (moderately to poorly sorted) and mean diameters of -0.5 and 2.9 phi (Table 1, Fig. 7a). Samples from the valley-confined and overbank deposits mostly plot in the same area (Fig. 7a), implying that

Table 1 Grain size parameters of the studied samples. Mean $_{\emptyset}$ = Mean diameter (phi), Md $_{\emptyset}$ = Median size particle (phi); σ_{\emptyset} = Sorting (phi), LL = Las Lajas barranca, Ce = Ceniza barranca, Se = Barranca Seca, Gu = Guacalate river, SMD=San Miguel Dueñas. See Fig. 1 for sample location. As defined by Walker (1983), F1 is the weight percent of the grain size distribution finer than 1 mm while F2 is the weight percent of the grain size distribution finer than 63 μ m.

			Matrix gra	in size distr	ibution (wt%	6) and GRA	DISTAT paran	neters (in ph	i scale)		
Sample	Unit	Sample location and type	Lapilli	Ash	F1	F2	Mean φ	Md φ	σφ	Skewness	Kurtosis
FG18-A6-BAF1	_	LL, Valley-Confined	33.37	66.63	71.10	20.10	-0.1	0.24	2.74	-0.15	0.86
FG18-B1-BAF1	_	Ce, Valley-Confined	35.37	64.63	66.61	20.91	-0.21	0.23	2.98	-0.16	0.77
FG18-B2-BAF1	-	Ce, Valley-Confined	31.83	68.17	53.10	16.26	-0.09	0.40	2.89	-0.20	0.85
FG18-C1-BAF1	-	Se, Valley-Confined	32.94	67.06	70.94	22.33	0.08	0.36	2.75	-0.14	0.84
FG18-A7-BAF3	mBLA7	LL, Valley-Confined	39.28	60.72	65.16	18.81	-0.42	-0.09	2.88	-0.12	0.75
FG18-A11-BAF4	mBLA6	LL, Valley-Confined	40.59	59.41	63.10	18.45	-0.36	-0.17	2.84	-0.06	0.71
FG18-A12-BAF5	mBLA5	LL, Valley-Confined	35.29	64.71	67.91	19.13	-0.24	0.18	2.81	-0.16	0.79
FG18-A13-BAF6	mBLA4	LL, Valley-Confined	28.56	71.44	73.75	21.03	0.06	0.48	2.72	-0.19	0.95
FG18-A14-BAF7	_	LL, Valley-Confined	31.72	68.28	65.24	19.68	-0.12	0.39	2.86	-0.21	0.84
FG18-A15-BAF8	-	LL, Valley-Confined	26.54	73.46	75.03	22.99	0.29	0.66	2.64	-0.19	0.97
FG18-A18-BAF9	mBLA3	LL, Valley-Confined	32.53	67.47	69.85	20.35	-0.13	0.30	2.82	-0.18	0.83
FG18-A19-BAF10	-	LL, Valley-Confined	30.76	69.24	71.72	21.13	-0.10	0.40	2.89	-0.21	0.90
FG18-A28-BAF12	mBLA2	Gu, Valley-Confined	30.94	69.06	71.26	21.31	-0.01	0.40	2.78	-0.18	0.86
FG18-A26-BAF11	mBLA1	Gu, Valley-Confined	30.94	69.06	56.20	16.80	-0.27	0.18	2.86	-0.17	0.75
FG18-A30-BAF13	mBLA-OB1	LL, Overbank	22.96	77.04	78.70	25.02	0.57	0.77	2.60	-0.18	1.08
FG18-A8-O1	mBLA-OB3	LL, Overbank	37.75	62.25	64.64	19.15	-0.44	0.08	2.97	-0.17	0.74
FG18-A9-O2	mBLA-OB4	LL, Overbank	32.68	67.32	71.76	20.85	0.06	0.28	2.67	-0.11	0.86
FG18-A10-O1	mBLA-OB3	LL, Overbank	37.15	62.85	62.85	11.81	-0.40	0.11	2.93	-0.18	0.75
FG18-A17-O2	mBLA-OB2	LL, Overbank	36.59	63.41	63.41	11.74	-0.46	0.13	2.98	-0.20	0.73
FG18-A20-O1	mLA-OB2	LL, Overbank	37.78	62.22	65.19	18.52	-0.55	0.03	3.01	-0.18	0.71
FG18-A23-O0	mBLA-OB1	LL, Overbank	20.65	79.35	79.35	17.18	0.78	0.95	2.45	-0.18	1.08
FG18-A25-O3	mBLA-OB1	LL, Overbank	30.31	69.69	73.94	20.13	-0.04	0.35	2.68	-0.19	0.94
FG18-A1-S2	csLA2	LL, Surge	0.82	99.18	99.18	50.82	2.92	3.03	1.31	-0.15	0.96
FG18-A2-S1	sLA1	LL, Surge	16.37	83.63	83.63	16.37	1.02	1.08	1.13	0.00	0.93
FG18-A4-S2	csLA2	LL, Surge	0.35	99.65	99.65	42.31	2.74	2.77	1.64	0.10	0.97
FG18-A3-S1	sLA1	LL, Surge	9.41	90.59	90.59	11.96	0.98	0.87	1.44	-0.14	0.91
FG18-A5-S2	sLA2	LL, Surge	1.28	98.72	82.11	50.80	2.65	2.77	2.97	-0.17	0.74
FG18-A21-ASC1	mLA2	LL, Surge	9.81	90.19	90.19	28.08	1.74	1.85	2.05	-0.16	1.01
FG18-A24-ASC1	mLA2	LL, Surge	17.53	82.47	82.47	17.73	0.97	0.93	2.15	-0.01	0.97
FG18-TEPHRA2	-	SMD, Fallout	5.3	94.7	88.88	12.37	0.99	0.26	1.87	0.53	1.34

overspilling here directly involved the main body of channeled PDCs. The F2 (wt% finer than 63 µm) versus F1 (wt% finer than 1 mm) diagram of Walker (1983) confirms the significant amount of fine ash (between 17 and 25 wt% for fractions ≥4 phi) in the matrix of both the valleyconfined and overbank PDC deposits (Fig. 7b), while some of the ashcloud surge deposits reach at least ~50 wt% of fines (≥ 4 phi). Following the stratigraphic relationships found inside the valleyconfined deposits (mBLA units in Fig. 6) and because sampling was performed systematically at the lobe front of each depositional unit, granulometric results of the valley-confined samples taken at each lobe front can be plotted against distance from the summit to investigate bulk grain-size evolution in Las Lajas. Using the statistics of the two lognormal grain-size sub-populations calculated by DECOLOG for each valley-confined lobate front unit (mBLA1 to mBLA 7 in Table 2 and Fig. 8), grain-size does not vary simply with distance in the fine subpopulations, however the mean particle diameter and sorting in the coarse sub-populations does vary significantly with distance (i.e., unit mBLA6 in Fig. 8a,b) . These results suggest that the proportion of the two sub-populations, identified here as peak grain sizes, within the matrix of the June 2018 PDC deposit sequence, are not correlated to each other. Moreover, since our sampling was mostly performed at the lobe front of each unit, such variations in the statistical parameters are representative of internal processes that occurred during the emplacement of the frontal PDC regions only.

The quantitative lithological component analysis carried out on fifteen PDC matrix samples via optical microscopy reveals noteworthy textural variations in terms of relative abundances of the eleven recognized lithological component categories (Fig. 9). Four main lithological components are identified among the selected samples, from the most abundant to the least: free crystals, partially red oxidized clasts, black scoria and oxidized clasts (Table 3 and Fig. 9a). Other components represent max. 6% in abundance of the total number of particles analyzed in each sample. However, some variations are found in terms

of relative abundances of some of these secondary components (grey clasts and hydrothermally altered clasts) inside the valley-confined PDC deposits (Table 3 and Fig. 9b). A similar approach as for the granulometry can be taken to investigate textural variations within the June PDC deposit sequence in Las Lajas barranca. Fig. 9a shows that while the abundance of free crystals does not vary between the valley-confined PDC units sampled, a near-inverse relationship is found between the fully oxidized and partially oxidized clast population in the proximal mBLA units (from mBLA7 to mBLA4), with a decrease in abundance of fully oxidized clasts (from 16% to 2%) while the partially oxidized clast abundance increases (from 16% to 28%) simultaneously. A progressive increase (of about 10%) in the abundance of black scoria with distance from the summit represents the only other significant lithological change among the main component categories recognized, with the remaining changes being visually secondary (Fig. 9b). The componentry of these secondary lithological groups mostly reveals a decrease in the abundance of grey clasts and hydrothermally altered clasts (of about 5% and 3%, respectively) from the proximal (mBLA7) to distal (mBLA1) valley-confined lobate front units (Fig. 9b). Valley-confined samples collected in the two other barrancas affected by the June 3rd PDCs (Ceniza and Seca) show similar componentry as the ones from Las Lajas, with a high abundance of free crystals and black scoria, but relatively low content of oxidized clasts (Table 3). As comparison, the componentry of the tephra fallout sample representing deposits from the sub-Plinian phase on June 3rd also shows a high content of free crystals, brown glass and black scoria, and paucity (< 0.5%) or absence of any other lithological component categories (Table 3).

2.5. Scanning electron microscopy

A representative number of particles (n = 155) from the 2 phi grain size fraction from five samples collected from the 2018 deposits were selected for Scanning Electron Microscopy. The instrument used for

Table 2 DECOLOG statistical parameters (in phi scale) of the polymodal matrix grain size distributions of the selected samples from June 3rd, 2018. $\sigma =$ Sorting (phi). See text for details.

Sample	Unit	Sample Type	Sub-population	Mean	Mode	Median	Variance	σ	Skewness	Kurtosis
T010 16 P4T1		V 11 0 C 1	1st lognormal (Coarse)	-2.73	-3.85	-3.17	3.44	1.86	1.75	8.90
FG18-A6-BAF1	-	Valley-Confined	2nd lognormal (Fine)	1.43	0.85	1.24	3.16	1.78	0.71	3.90
FG18-A7-BAF3	mBLA7	Valley-Confined	1st lognormal (Coarse)	-2.93	-4.19	-3.44	3.83	1.96	2.48	15.59
FG18-A/-DAF3	IIIDLA/	vaney-Commed	2nd lognormal (Fine)	1.45	0.82	1.23	3.22	1.79	0.77	4.07
FG18-A11-BAF4	mBLA6	Valley-Confined	1st lognormal (Coarse)	-0.76	-3.56	-1.94	18.23	4.27	3.04	22.99
rG18-A11-DAF4	IIIDLAO	vaney-Commed	2nd lognormal (Fine)	0.91	1.86	1.27	2.62	1.62	-1.75	8.87
FG18-A12-BAF5	mBLA5	Valley-Confined	1st lognormal (Coarse)	-3.85	-3.59	-3.76	0.84	0.91	-0.60	3.65
FG18-A1Z-DAF5	IIIDLAS	vaney-Commed	2nd lognormal (Fine)	1.26	0.59	1.03	3.71	1.93	0.76	4.05
FG18-A13-BAF6	mBLA4	Valley-Confined	1st lognormal (Coarse)	-3.80	-3.46	-3.68	0.92	0.96	-0.77	4.06
rG18-A13-DAF0	IIIDLA4	vaney-Commed	2nd lognormal (Fine)	1.31	0.62	1.08	3.52	1.88	0.82	4.23
FG18-A14-BAF7		Valley-Confined	1st lognormal (Coarse)	-4.07	-4.02	-4.05	0.15	0.39	-0.30	3.16
FG18-A14-DAF/	_	vaney-Commed	2nd lognormal (Fine)	1.29	0.62	1.06	3.71	1.93	0.76	4.04
EC10 A10 DAE0	DIAO	Valley Confined	1st lognormal (Coarse)	-3.90	-3.69	-3.82	0.77	0.88	-0.50	3.45
FG18-A18-BAF9	mBLA3	Valley-Confined	2nd lognormal (Fine)	1.30	0.62	1.06	3.73	1.93	0.76	4.06
EC10 A00 DAE10	DI A O	V-11 C C 1	1st lognormal (Coarse)	-2.83	-3.95	-3.26	3.32	1.82	2.04	11.21
FG18-A28-BAF12	mBLA2	Valley-Confined	2nd lognormal (Fine)	1.52	0.93	1.32	3.05	1.75	0.75	4.01
FG18-A26-BAF11	mBLA1	Valley-Confined	1st lognormal (Coarse)	-3.76	-3.48	-3.66	0.93	0.96	-0.62	3.68
FG18-A20-DAF11	IIIDLAI	vaney-Commed	2nd lognormal (Fine)	1.35	0.69	1.12	3.67	1.91	0.76	4.03
EC10 A0 O1	mBLA-OB3	011-	1st lognormal (Coarse)	-3.33	-4.49	-3.82	3.13	1.77	3.04	30.00
FG18-A8-O1	mblA-OB3	Overbank	2nd lognormal (Fine)	1.48	0.83	1.25	3.28	1.81	0.80	4.16
EC10 40 00	DI A OD 4	011-	1st lognormal (Coarse)	-2.30	-1.25	-1.92	4.02	2.00	-1.37	6.54
FG18-A9-O2	mBLA-OB4	Overbank	2nd lognormal (Fine)	2.00	1.56	1.85	2.42	1.55	0.60	3.65
EC10 A10 O1	DI A OD2	Overbank	1st lognormal (Coarse)	-3.17	-4.42	-3.70	3.65	1.91	3.04	23.00
FG18-A10-O1	mBLA-OB3	Overbank	2nd lognormal (Fine)	1.46	0.84	1.24	3.10	1.76	0.78	4.09
EC10 A17 00	DI A ODO	011-	1st lognormal (Coarse)	-3.68	-4.60	-4.07	1.97	1.40	3.04	23.00
FG18-A17-O2	mBLA-OB2	Overbank	2nd lognormal (Fine)	1.40	0.74	1.17	3.26	1.81	0.82	4.21
EG10 A00 O1	I A ODO	011-	1st lognormal (Coarse)	-4.10	-4.73	-4.37	0.93	0.97	3.04	23.00
FG18-A20-O1	mLA-OB2	Overbank	2nd lognormal (Fine)	1.28	0.52	1.02	3.70	1.92	0.91	4.49
EG10 400 00	DI A OD1	011-	1st lognormal (Coarse)	-2.64	-3.89	-3.11	4.30	2.07	1.89	9.97
FG18-A23-O0	mBLA-OB1	Overbank	2nd lognormal (Fine)	1.62	1.05	1.42	3.18	1.78	0.69	3.87
EC10 ADE O0	DI A OD1	011-	1st lognormal (Coarse)	-4.08	-3.98	-4.05	0.16	0.40	-0.523	3.50
FG18-A25-O3	mBLA-OB1	Overbank	2nd lognormal (Fine)	1.09	0.41	0.86	3.73	1.93	0.78	4.10
EC10 A001	aT A 1	Carron	1st lognormal (Coarse)	-0.35	0.61	0.01	2.30	1.73	-1.52	7.38
FG18-A2S1	sLA1	Surge	2nd lognormal (Fine)	2.90	2.67	2.83	1.08	1.04	0.46	3.38
EG10 TERMINAS		P-11	1st lognormal (Coarse)	0.04	-0.10	-0.01	0.48	0.70	0.41	3.30
FG18-TEPHRA2	_	Fallout	2nd lognormal (Fine)	4.06	3.99	4.03	0.16	0.40	0.38	3.25

these analyses is a Topcon Aquila compact scanning electron microscope (SEM) with a 50,000× magnification, integrated with an optical microscope of 30× magnification for optical mapping and imaging in color. Sample preparation included placing individual particles on dry mounts and sputter coating to improve SEM imaging on low conductivity samples by increasing the number of secondary electrons that can be detected from the surface of the sample in the SEM, and therefore increasing the signal to noise ratio. Four out of the five samples selected were from PDC deposits in Las Lajas (one from the overbank unit mBLA-OB1 and one from the valley-confined unit mBLA7), Ceniza and Seca barrancas (Table 4). The fifth sample is a tephra fallout sample from the sub-Plinian phase that occurred on the morning of June 3rd. In addition, a sixth sample, named FGO17, is a tephra sample from a paroxysmal eruption that took place on January 26th, 2017, collected at the Fuego Volcano Observatory (OVFGO), in the town of Panimache (SW of Fuego; Fig. 1). This older sample was compared to the 2018 one in order to determine differences or similarities between the tephra deposits produced by two explosive events of different eruptive magnitude and style.

Each sample was described in terms of vesicularity (volume of vesicles) (Heiken and Wohletz, 1985), shape, and surface. For vesicular grains, vesicles were measured using the program GIMP (GNU Image Manipulation Program). Each vesicle was measured in terms of width and length, and an average size per sample grain was calculated based on those measurements (sizes varied between 6 and 208 μm). The number of vesicles per grain varied between 0 and 16 and the vesicularity of each grain was classified as low (0–30%), moderate (30–60%) and high (60–100%). The shape of the grains was classified with the terms blocky, angular, fluid, or inter-vesicular walls (IVW) as per Bustillos et al. (2018). Blocky grains contain planar to curviplanar surfaces

and can also have a tabular or prismatic form (Heiken and Wohletz, 1985). Angular grains are characterized by having pointy or sharp edges, fluid grains tend to be spherical or tear shaped (Bustillos et al., 2018). In terms of surface, the following terms were used: smooth, rugged, molten, broken, planar, fractured, and jagged. Rugged textures are characterized by having corrugations, molten - also referred to as fluid in literature (e.g., Heiken and Wohletz, 1985) - exhibit textures that appear to have solidified after being melted, and jagged grains exhibit rough or sharp edges. Based on the lithological components identified (see previous section), for this study, the two components selected for SEM analyses of the PDC samples were the black scoria and grey clasts, whereas for the tephra fallout samples, black and brown glasses were also analyzed. Free crystals and lithics in each sample were also imaged for reference. Results of the qualitative textural classification of each sample in terms of vesicularity, shape and surface characteristics are presented in Table 4. Some examples of SEM images obtained as well as the results of measured averaged vesicle size per sample grain are shown in Fig. 10.

The June 2018 PDC samples are characterized by low to moderate vesicularity, with many grains having no vesicles, or at least not visible due to adhering dust, while others contain only a few vesicles (Table 4 and Fig. 10). The shape of the grains is mostly blocky and angular, but fluid shapes are also common. In terms of surface, most grains exhibit mainly a smooth surface, but with some rugosity present in parts of the grain. Some of the grains are also broken, jagged and/or fractured, and others contain planar surfaces. In addition, many of the grains contain adhering dust on their surfaces. There are some differences among the PDC samples. For instance, the sample collected inside the Ceniza barranca (FG18-B2-BAF1) is characterized by low- to moderate vesicularity,

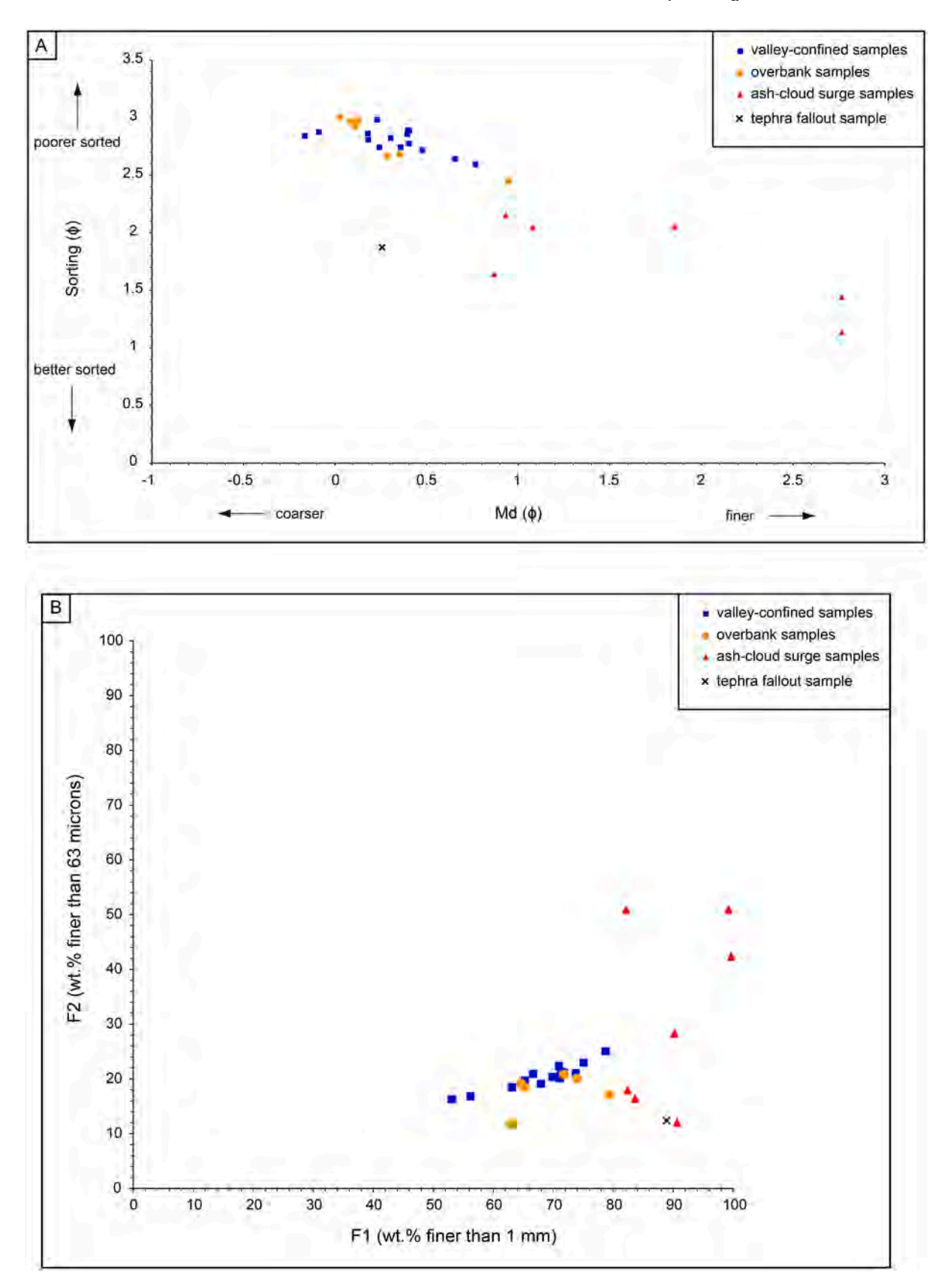
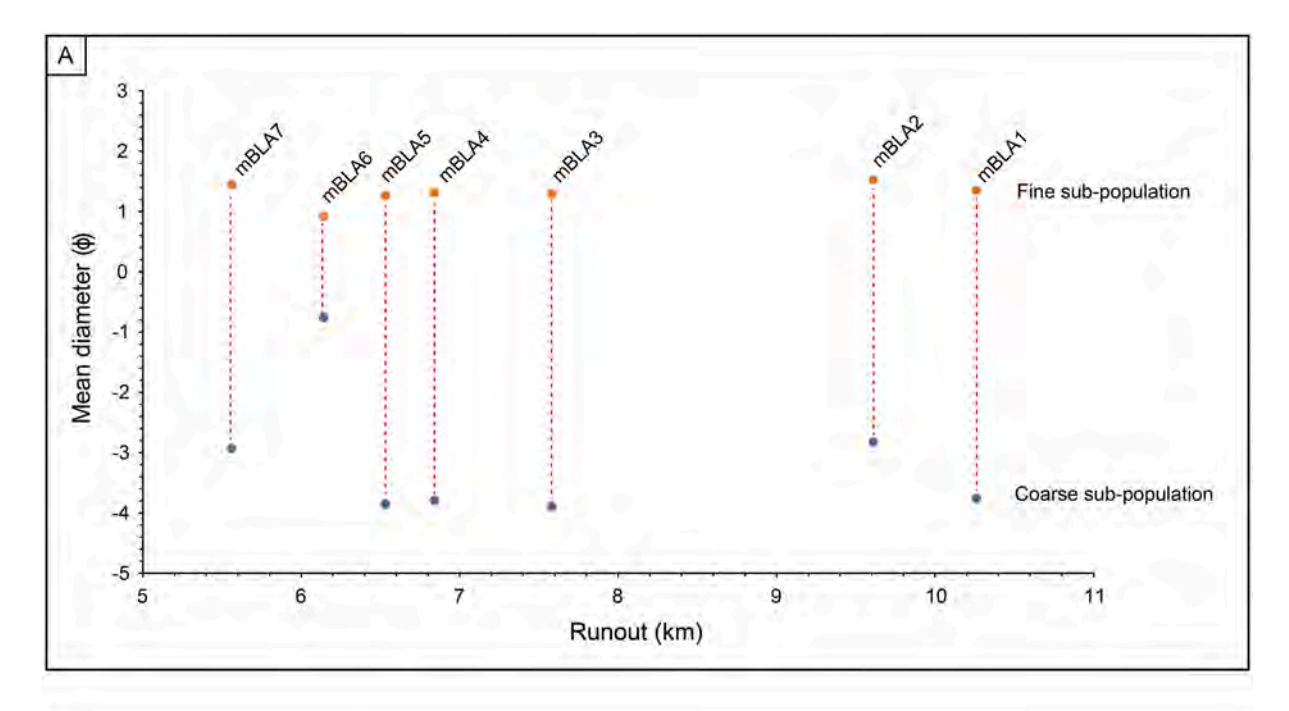


Fig. 7. A) Plot of median diameter (Md_0) versus sorting coefficient (σ_0) for the different 2018 PDCs and tephra fallout deposits. B) Plot of the weight percent finer than 63 μ m (F2) versus the weight percent finer than 1 mm (F1) for the different 2018 PDC and tephra fallout deposits.



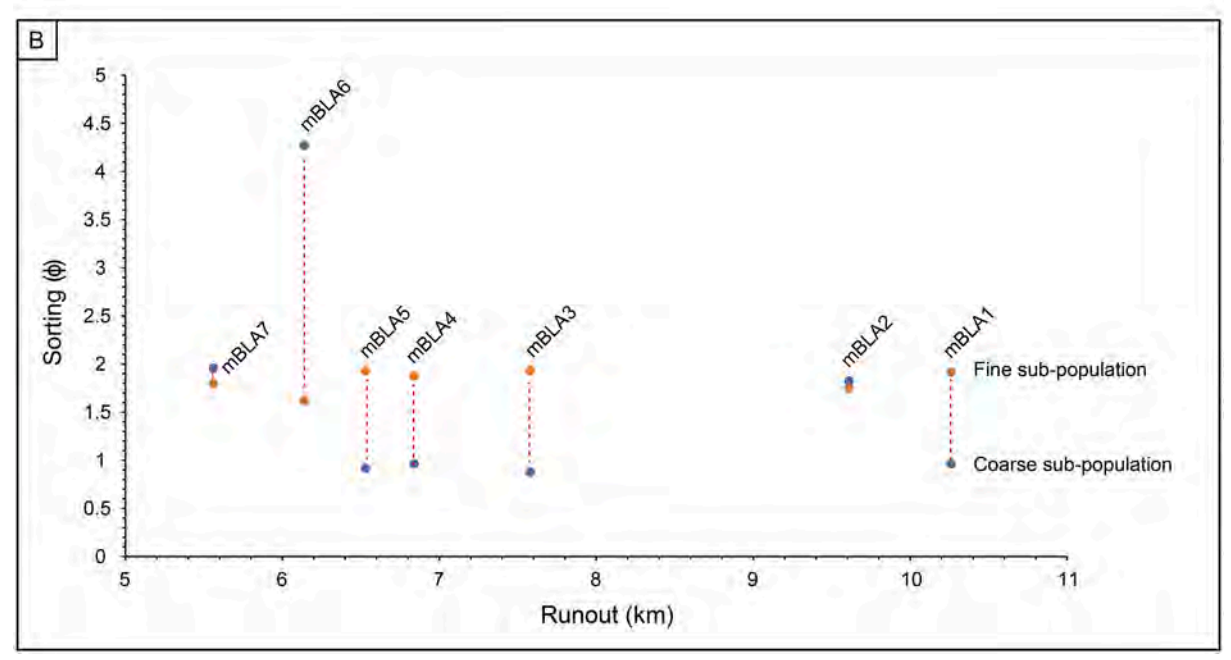


Fig. 8. Results from deconvolution of the polymodal distributions inside each valley-confined lobate front 2018 PDC unit sampled inside Las Lajas barranca showing variations of A) mean diameter and B) sorting (in phi unit) of both the fine and coarse sub-populations as a function of the runout distance of each PDC unit.

blocky and angular grains with smooth and rugged surfaces, and conchoidal fractures. This sample, along with the sample collected inside barranca Seca (FG18-C1-BAF1), has the highest vesicularity among the 2018 PDC samples (Fig. 10).

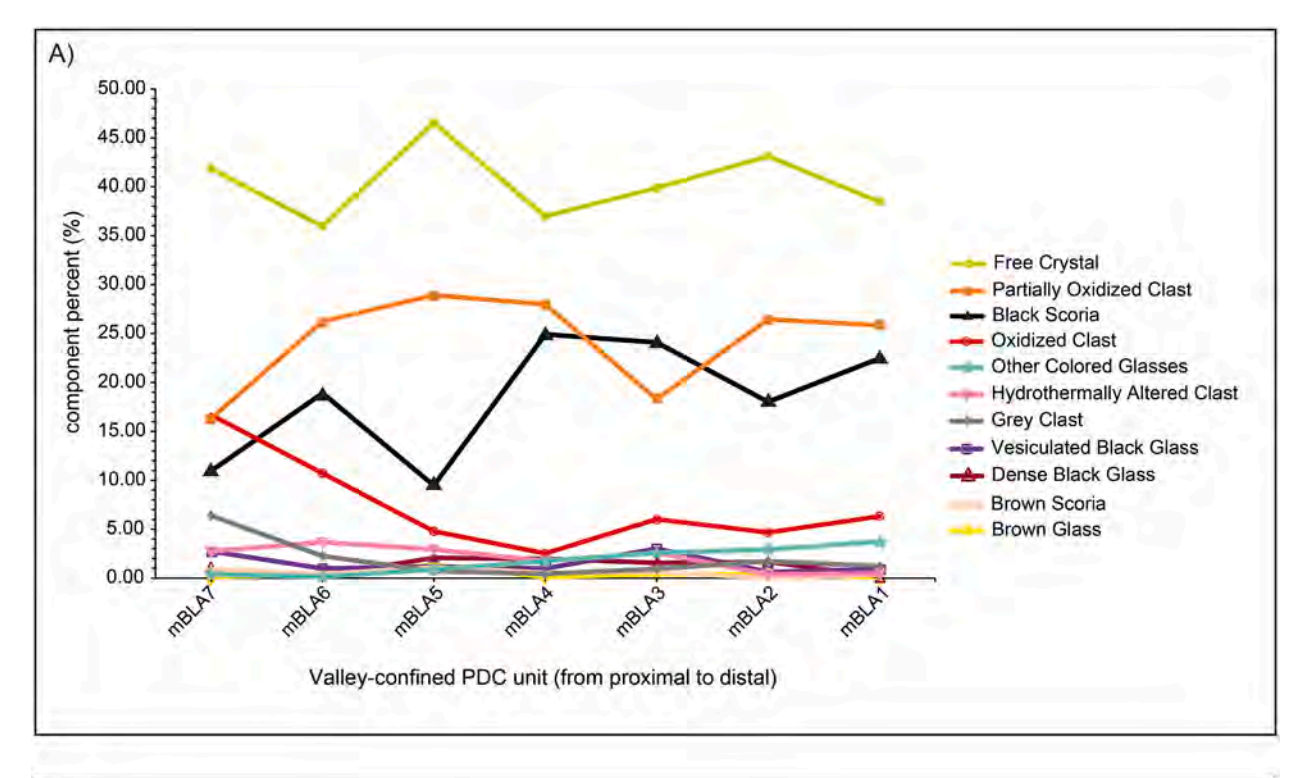
The two tephra fallout samples analyzed, in comparison to the PDC samples, have a wider range of vesicularity. Almost all particles analyzed have vesicles, ranging from low to high vesicularity (Table 4 and Fig. 10). In general, the shape of the grains is mostly blocky and/or angular, but fluid shapes are also common (sample FGO17). There is a variety of surface textures, but jagged, rugged, and smooth surfaces are the most common. Adhering dust is also found on some of the grains. Particles from the 2018 sub-Plinian fallout have a higher vesicularity, a larger range in vesicle sizes (Fig. 10), and many have larger vesicles than particles from the 2017 tephra fallout, which have low to moderate

vesicularity and mostly smooth, fluid or molten surface textures, indicative of rapid cooling of a low viscosity magma.

3. Discussion

3.1. Juvenile versus accidental lithics in the June 3rd, 2018 PDC deposits

Results obtained from the quantitative lithological component analysis and qualitative SEM textural classification carried out on matrix samples from the June 2018 PDC and tephra fallout deposits show strong relative abundance and textural variations, both between the different barrancas affected by the 2018 eruption (mainly Ceniza, Seca and Las Lajas), and within the different PDC units emplaced in Las Lajas on the afternoon of June 3rd (mLBA1 to mBLA7). Such variations can be



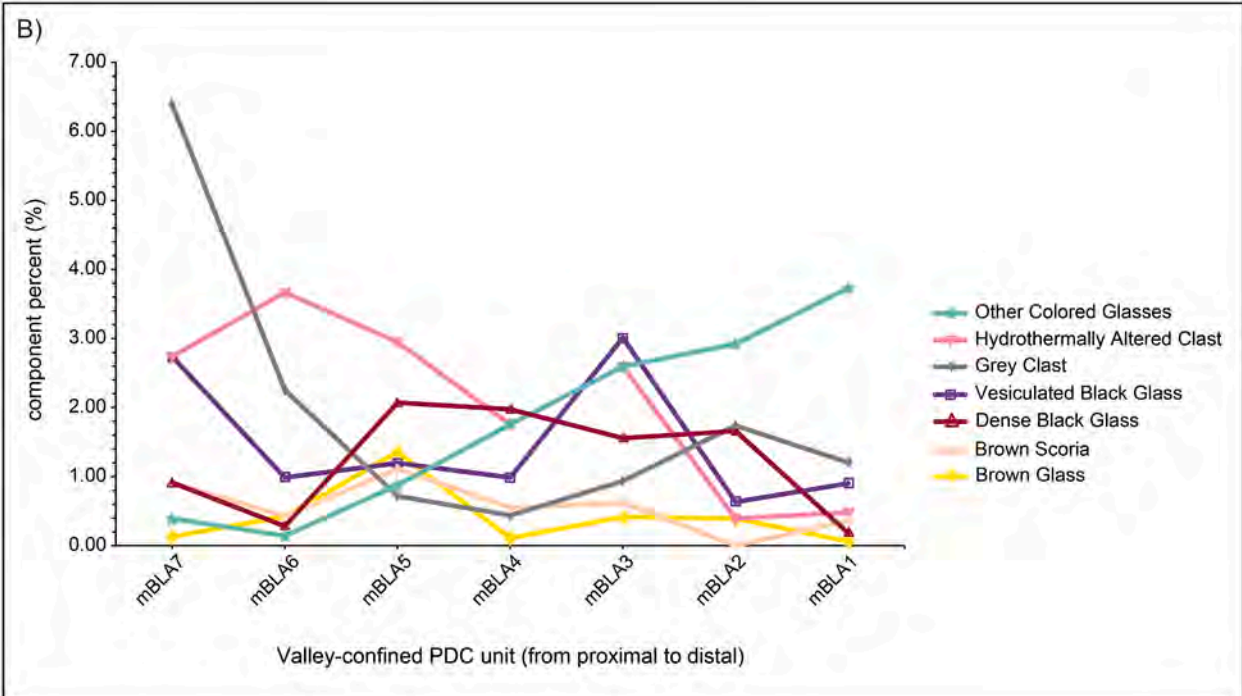


Fig. 9. Componentry results inside each valley-confined lobate front 2018 PDC unit sampled inside Las Lajas barranca showing variations of A) all lithological components and B) secondary lithological components only, as a function of distance from summit.

indicative of the various contributions of material from the explosive events directly (i.e., juvenile material), but also from the erosion and remobilization of the 'perched' pyroclastic material that rapidly accumulated on the southeastern upper flank (i.e., accidental lithics) during the previous paroxysm eruptions in the last few months prior to the June 2018 events (Albino et al., 2020; Naismith et al., 2019). Most clasts analyzed from PDC deposit matrices of June 3rd are characterized by an overall blocky shape, smooth textures with some rugosity, and low to moderate vesicularity. In contrast, the tephra fallout sample from the

sub-Plinian phase has a moderate to high vesicularity and are mainly blocky and angular in shape, with jagged surfaces.

The abundance of fresh, brown glass and black scoriae in both tephra samples from January 2017 and June 2018, confirms the juvenile nature of these components. Both the high abundance of black scoria and low content of fully oxidized clasts found inside the distal valley-confined PDC deposit samples from Las Lajas (units mBLA1 and mBLA2), as well as from those collected in the two other barrancas affected by the June 3rd PDCs (Ceniza and Seca) suggest that these PDCs contained

What of Voicanbiogy and Geomethian Research 430 (2023) 10779

Table 3
Componentry data (in abundance %) of the 1 phi grain-size fraction of the studied samples. LL = Las Lajas barranca, Ce = Ceniza barranca, Se = Barranca Seca, Gu = Guacalate river, SMD = San Miguel Dueñas. See text for details.

					Componentry (%	o) of the 1	phi grain-s	ize fraction					
Sample	Unit	Sample Location and Type	Brown Glass	Dense Black Glass	Vesicu-lated Black Glass	Black Scoria	Brown Scoria	Free Crystal	Oxidized Clast	Partially Oxidized Clast	Hydroth-ermally Altered Clast	Grey Clast	Other Color- ed Glasses
FG18-A6-BAF1	_	LL, Valley-Confined	0.9	1.1	0.9	8.1	1.1	42.5	11.4	26.5	3.1	4.3	0.1
FG18-B1-BAF1	-	Ce, Valley-confined	1.7	0.8	2.4	17.9	3.3	46.4	5.4	13.5	1.3	5.2	2.1
FG18-B2- BAF1	-	Ce, Valley-confined	0.5	0.2	1.4	20.4	0.2	45.8	2.3	22.2	0.8	2.6	3.6
FG18-C1-BAF1	-	Se, Valley-confined	0.1	0.2	1.3	31.3	1.1	43.0	5.2	11.1	1.5	3.7	1.5
FG18-A7-BAF3	mBLA7	LL, Valley-Confined	0.1	0.9	2.7	11.0	0.9	41.9	16.7	16.3	2.7	6.4	0.4
FG18-A11- BAF4	mBLA6	LL, Valley-Confined	0.4	0.3	1.0	18.9	0.4	36.0	10.7	26.2	3.7	2.3	0.1
FG18-A12- BAF5	mBLA5	LL, Valley-Confined	1.3	2.1	1.2	9.5	1.1	46.5	4.8	28.9	3.0	0.7	0.9
FG18-A13- BAF6	mBLA4	LL, Valley-Confined	0.1	2.0	1.0	25.0	0.5	37.0	2.5	28.0	1.8	0.4	1.7
FG18-A14- BAF7	-	LL, Valley-Confined	0.4	0.9	0.7	22.0	0.6	42.5	6.2	24.1	0.9	0.6	1.1
FG18-A14- BAF8	-	LL, Valley-Confined	0.5	0.5	4.3	7.3	1.5	54.5	6.0	17.4	3.4	3.3	1.3
FG18-A18- BAF9	mBLA3	LL, Valley-Confined	0.4	1.6	3.0	24.1	0.6	39.9	6.0	18.3	2.6	0.9	2.6
FG18-A19- BAF10	-	LL, Valley-Confined	0.1	0.4	2.7	24.1	0.0	32.1	8.1	25.4	1.8	2.7	2.6
FG18-A28- BAF12	mBLA2	Gu, Valley-Confined	0.4	1.7	0.6	18.0	0.0	43.1	4.7	26.5	0.4	1.7	2.9
FG18-A26- BAF11	mBLA1	Gu, Valley-Confined	0.1	0.2	0.9	22.5	0.3	38.5	6.3	25.8	0.5	1.2	3.7
FG18-A30- BAF13	mBLA- OB1	LL, Overbank	0.0	0.4	0.6	19.0	0.2	41.7	2.7	25.8	1.7	5.9	2.0
FG18- TEPHRA2	-	SMD, Fallout	21.9	0.0	0.5	7.4	0.0	65.9	0.4	0.0	0.0	0.0	3.9

Clast textural data (in abundance %) obtained by SEM analyses on the 2 phi grain-size fraction of each studied sample. LL = Las Lajas barranca, Ce = Ceniza barranca, Se = Barranca Seca, Gu = Guacalate river, SMD = San Miguel Dueñas, OVFGO = Fuego Volcano Observatory. See text for details

		,		SE	M textural cl	SEM textural classification of the 2 phi grain-size fraction	the 2 phi gr	ain-size fra	ction						
Sample	Sample Location and Type		Vesicularity			Shape	0)				33	Surface texture			
		Low	Low Moderate	High	Blocky	Angular	Fluid	IVW	Smooth	Rugged	Broken	Molten	Planar	Fractured	Jagged
FG18-B2- BAF1	Ce, Valley-confined PDC	20	20	10	80	30	20	0	100	20	20	0	09	40	10
FG18-C1-BAF1	Se, Valley-confined PDC	80	20	20	100	20	0	0	20	100	09	0	09	40	40
FG18-A7-BAF3	LL, Valley-Confined PDC	100	0	0	80	20	30	0	80	80	40	20	30	20	0
FG18-A30-BAF13	LL, Overbank PDC	06	10	10	80	30	20	10	70	100	40	0	40	0	30
FG18-TEPHRA2	SMD, Fallout	38	34	41	72	41	7	0	31	45	28	0	10	21	55
FG017	OVFGO. Fallout	73	27	7	40	53	29	13	80	20	7	29	13	27	40

mostly particles from the June 3rd and recent (2015 to February 2018?) paroxysm eruptions in their solid fraction. In contrast, the high abundance of oxidized and old lava fragments (dense grey clasts) together with the lower content of black scoria inside the top valley-confined units of the June 3rd PDC sequence (units mBLA6 and mBLA7) indicate that these PDCs contained mostly clasts from older (pre-2015?) paroxysm eruptions in their solid fraction. We suggest that the progressive increase in the abundance of fully oxidized clasts and decrease of black scoria within the June 3rd valley-confined PDC sequence in Las Lajas (from mBLA1 to mBLA7) indicate a higher proportion of old, 'perched' pyroclastic material with time, which progressively became the main source of solid fraction inside PDCs generated after 3.30 pm on June 3rd (see next section).

Based on these results, the eleven lithological components recognized here are tentatively grouped into three main categories: free crystals, juveniles and accidental lithics (Fig. 11). The juvenile category here regroups clasts erupted during recent (2015-February 2018) paroxysms including the June 2018 event, and comprises brown and black glasses and scoriae, while accidental lithics correspond to clasts erupted during older (pre-2015) paroxysm eruptions and contain partially/fully oxidized clasts, hydrothermally altered clasts and dense grey clasts. In this classification, the degree of clast oxidization and hydrothermal alteration is thought to be correlated with the time the clast spent in contact with hot, humid atmospheric gases (Martínez-Martínez et al., 2023), i.e., the time it was stored inside the 2015 collapse structure containing 'perched' pyroclastic material on the proximal southeastern flank of Fuego (see next section). The dense grey clasts could correspond to old lava fragments from the upper flanks that were eroded and/or picked up during PDC generation and/or transport over the steep, proximal upper slopes. Following this classification, as inferred from the componentry results, we can observe a progressive decrease of juvenile material and increase of accidental lithics from bottom to top within the June 3rd valley-confined PDC deposit sequence in Las Lajas, especially from units mBLA4 to mBLA7 (Fig. 11). Juvenile content inside the valley-confined lobate front PDC units varies in abundance from 16% to 32%, accidental lithics from 28% to 43%, and free crystals from 36% to 47% (Fig. 11). The highest content of free crystals is found inside the tephra fallout sample from the sub-Plinian phase on June 3rd with \sim 66% in abundance (Table 3).

3.2. Generation and emplacement mechanisms of the June 3rd, 2018 PDCs

3.2.1. PDC generation

The source mechanisms responsible for the generation and emplacement of the June 3rd, 2018, PDCs have been discussed in recent papers (Albino et al., 2020; Risica et al., 2022). Using TanDEM-X DEM differencing, Albino et al. (2020) obtained a thickness map for the PDCs, showing material loss in the upper portions of Las Lajas due to gravitational collapse and significant substrate erosion. They suggest that 'the eroded material in the upper slopes of the southeastern flank increased the volume of the flows (bulking) and likely caused the run-out distance of the 2018 PDCs to be larger than previous eruptions (1999-2017)'. Risica et al. (2022) used paleomagnetic analysis to show that 'the PDCs mostly derived from collapse of loose and partly hot pyroclastic deposits, stored high on the volcano, that had gradually accumulated there during the last 2+ years. They inferred that progressive collapse of these unstable deposits supplied the PDCs, causing a bulk-up process, waxing flow, channel overspill and unexpected runout, and each collapse had a larger volume and mass flux than the preceding one.' While we agree with these interpretations, the multi-faceted approach presented here by combining stratigraphic surveys, sedimentological and textural analyses of the PDC deposits, not only allows us to discuss in more details the processes that caused PDC generation and emplacement during the 2018 eruption, but also to reconstruct more fully the sequence of events that happened on June 3rd:

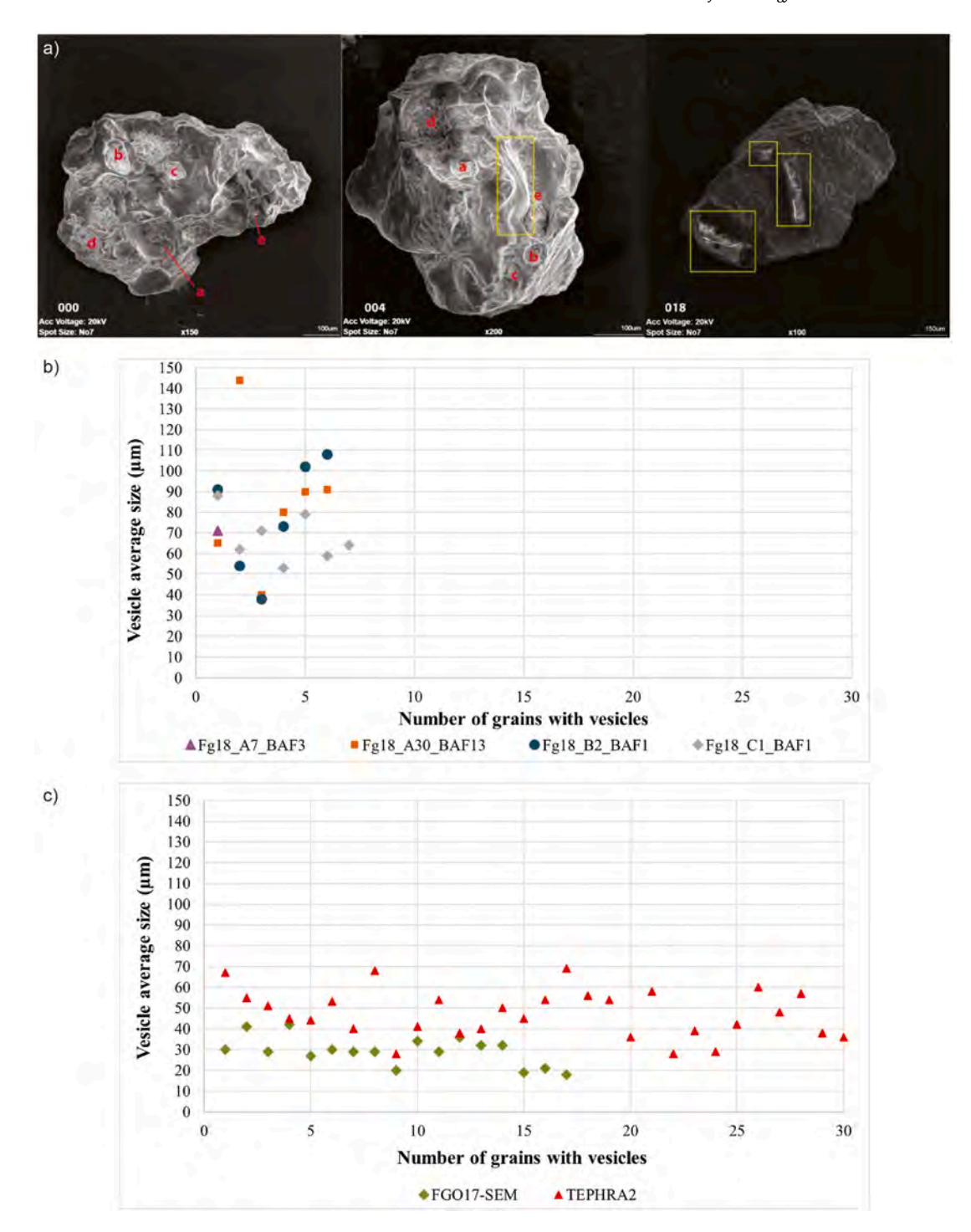


Fig. 10. Results of SEM analysis showing a) examples of SEM images obtained on three different lithological components (a-c) with red letters indicating vesicles and yellow rectangles delineating crystals. b) number of grains per sample containing vesicles and their average vesicle sizes for three samples collected inside the valley-confined 2018 PDC depositional units in Las Lajas (FG18-A30-BAF13), Ceniza (FG18-B2-BAF1) and Seca (FG18-C1-BAF1) barrancas. c) number of grains per sample containing vesicles and their average vesicle sizes for two tephra fallout deposit samples collected in January 2017 (FG017) and June 3rd, 2018 (TEPHRA2). (For interpretation of the references to color in this figure legend, the reader is referred to the web version of this article.)

- 1) The PDC deposit stratigraphy presented in Fig. 6 corresponds to deposits emplaced in the Las Lajas barranca between 3.00 pm and 4.30 pm on June 3rd. Based on their stratigraphic positions and lobe front distances from the summit, units mBLA1 and mBLA2, as well as mBLA-OB1 and m(B)LA-OB2, were emplaced during the peak of PDC activity between 3.00 and 3.30 pm, while units mBLA3-mBLA7 (and mBLA-OB3 mBLA-OB4) were emplaced during the PDC waning phase until 4.30 pm. Deposits from earlier PDCs that occurred in the
- morning until 2.30 pm were not exposed at this time and therefore not documented in this work. Only the three samples collected in the Seca and Ceniza barrancas (B1, B2 and C1 in Tables 1 and 3) could correspond to PDC deposits emplaced during the peak of the sub-Plinian phase around 1.00 pm;
- 2) The high content of juvenile material and low content of accidental lithics found inside units mBLA1 and mBLA2 in Las Lajas and in those sampled in Seca and Ceniza barrancas, as well as the pristine surface

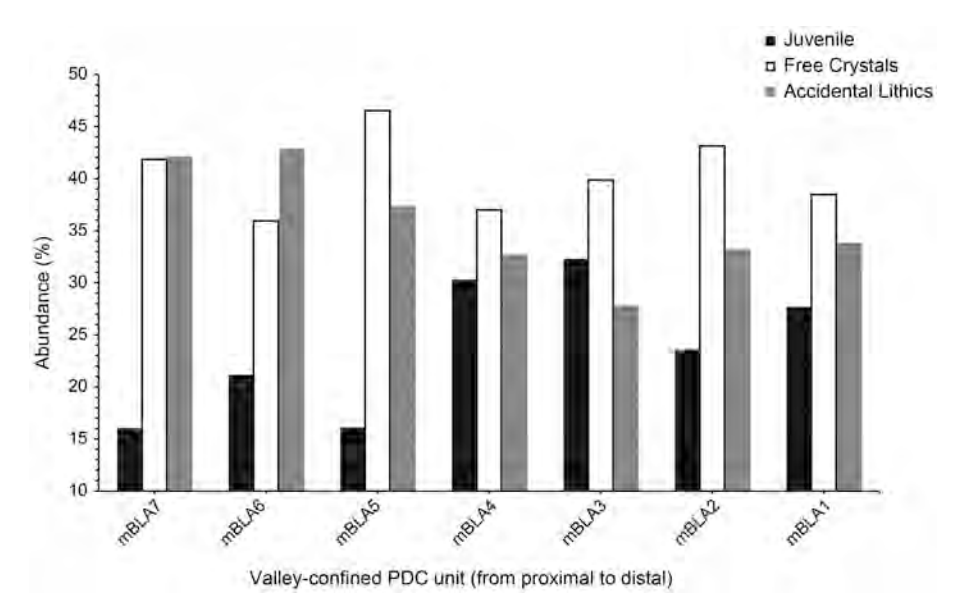


Fig. 11. Relative abundance (%) of juvenile, free crystals and accidental lithics inside each valley-confined lobate front 2018 PDC unit sampled inside Las Lajas barranca as a function of distance from summit.

textures of clasts collected in these samples (i.e., fresh dark grey crystal-ich andesite), suggest that these PDCs were generated either from column collapse (most likely scenario for PDCs emplaced in Seca and Ceniza around 1.00 pm) or gravitational collapse of freshly deposited, hot and unstable perched pyroclastic material located on the head scarp of barrancas (most likely source of the Las Lajas PDCs between 3.00 and 3.30 pm). Such freshly pyroclastic material could mostly consist of black scoria and partially oxidized (due to their short residence time) clasts, the two most abundant components in these units (Fig. 9 and Table 3). In the case of units mBLA1 and mBLA2 (and mBLA-OB1 - m(B)LA-OB2) in Las Lajas, both triggering mechanisms could have occurred simultaneously: strong summit explosions could have ejected ballistics that landed on top of the loose, hot surface made of perched tephra accumulated earlier during the sub-Plinian phase. Intense fallout of coarse pyroclasts on steep upper slopes has already been invoked to account for avalanching and formation of PDCs at Mount Fuji (Japan) that travelled >8 km (Yamamoto et al., 2005). Through their repeated and frequent impacts, the ballistics could have formed large, continuous headwall failures and triggered retrogressive, gravitational collapses of a thick and large portion of the 'perched' pyroclastic material to generate the most voluminous PDCs (Fig. 12);

3) The low content of juvenile (post-2015) material, as well as the blocky shape, smooth textures and low vesicularity found inside most juvenile clasts of units mBLA5-mBLA7 in Las Lajas, indicate that the associated PDCs were triggered mostly by small gravitational collapses of the colder, deeper portion of the pyroclastic material that accumulated during the period 2015–2018, triggering partial erosion of the headwalls and basement of the substratum that constitutes the upper southeastern flank of Fuego (Fig. 12), therefore increasing the proportion of accidental lithics inside their solid fractions. The smaller mean diameter and better sorting found inside the coarse sub-populations of units mBLA6 and mBLA7 (Fig. 8 and Table 2) could also suggest that a more homogeneous, smaller portion of the 'perched' pyroclastic material was involved in these two late PDC events. Such source mechanisms for the PDCs occurred during the waning phase of activity, between 3.30 pm and 4.30 pm.

Based on these correlations, we propose a conceptual model of PDC generation for the June 3rd events in the Las Lajas barranca (Fig. 12). This model consists of various temporal longitudinal and cross-sections

of the upper part of the southeastern flank of Fuego, upstream of the head of the Las Lajas barranca, that showed accumulation of pyroclastic materials during the period 2015–2018 (Albino et al., 2020; Risica et al., 2022). Each section represents a conceptual model of the topographic profile and infilling material inside the previously formed collapse structure at a particular location and time during the June 3rd events. Temporal sections are represented as isochrones (red outlines in Fig. 12) and are labelled T1, T2 and T3. For each section, the T1 isochrone corresponds to the loose, hot surficial portion of perched tephra and ballistics accumulated a few hours earlier during the sub-Plinian phase. T2 isochrone outlines the hot, thick and large portion of the pyroclastic material accumulated during the last paroxysms of Fuego, as well as parts of the headwalls and basement of the collapse structure already formed before 2015, which all collapsed gravitationally and retrogressively (including portions of T1) during the peak of PDC activity between 3.00 and 3.30 pm. T3 isochrone indicates the colder, deeper portion of the pyroclastic material that probably accumulated during the 2015–2018 paroxysms, as well as a larger portion of the lower headwalls and basement of the old collapse structure, which collapsed gravitationally during the waning PDC phase between 3.30 pm and 4.30 pm. In this model, each gravitational failure and collapse occurred independently but retrogressively, tapping the rapidly accumulated pyroclastic mass in the old collapse structure from the top to the base and front to the rear (Fig. 12). While the smaller and most superficial collapse events do not always generate PDCs, each package of material involved in the major failure events (T1-T3) correspond to the emplacement of a series of valley-confined PDC units downstream the Las Lajas channel (mBLA1mBLA7). This model shows some similarities with the model proposed by Risica et al. (2022) but differs in the following aspects: 1) headwall failures and gravitational collapses are not continuous, and we do not infer that they increase in size, volume and frequency with time; in contrast they are correlated with specific stratigraphic, sedimentological and textural characteristics of the valley-confined PDC units emplaced downstream of the Las Lajas barranca; 2) headwall failures and gravitational collapses do not exclusively include accumulated pyroclastic material from the period 2015-2018, but also sub-Plinian tephra and ballistics accumulated a few hours earlier, as well as portions of the old collapse structure present before 2015, including some fragments of lava flows that formed the upper part of the southeastern flank of Fuego, and found inside the valley-confined PDC units (i.e. dense grey clasts); 3) the duration of individual granular collapse event do not reflect the duration

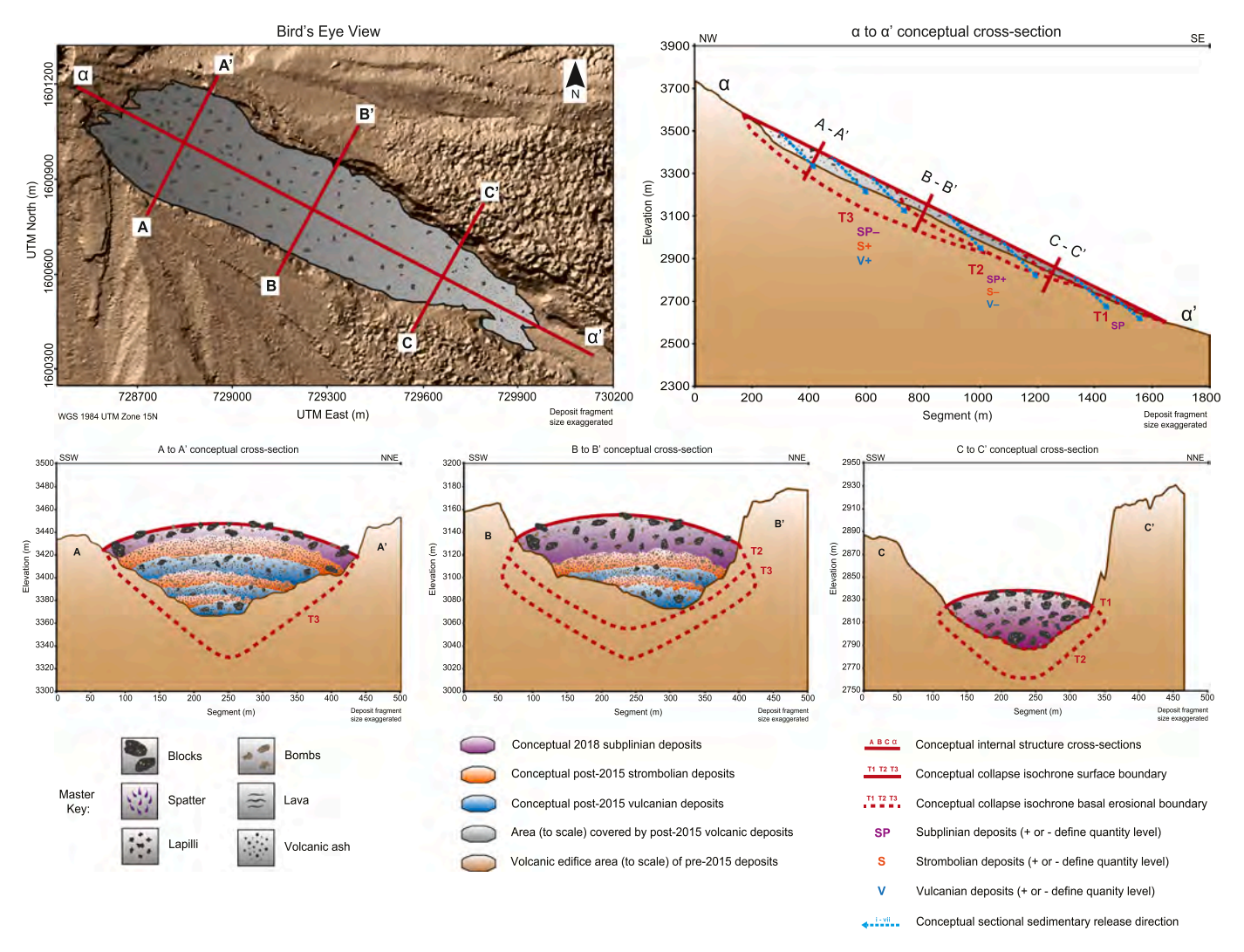


Fig. 12. Conceptual model of PDC generation for the June 3rd, 2018, events showing a bird's eye view, one longitudinal section and three cross-sections along the upper part of the southeastern flank of Fuego, upstream of the head of the Las Lajas barranca, that was affected by rapid accumulation of various lava flows and pyroclastic materials during the period 2015–2018. Each section represents a conceptual model of the topographic profile and infilling material inside the previously formed collapse structure at a particular location and time during the June 3rd events. See text for details.

of each PDC pulse but rather serve as a proxy for the mobility of the triggered series of PDCs.

3.2.2. PDC emplacement

Seventeen stratigraphic units have been recognized in the Las Lajas barranca and its surroundings and, based on detailed mapping, surface characteristics, lithofacies analysis, grain size distribution, componentry and clast surface texture, interpreted to belong to the June 3rd, 2018 events. In addition, two other PDC units in the Seca and Ceniza barrancas have been associated to these events. The three types of PDC deposits identified and mapped (valley-confined, overbank and ashcloud surge), and their associated five main lithofacies, are characteristics of long-runout, block-and-ash flow (BAF) deposits. Such deposits have already been studied elsewhere, like at Merapi during the 2006 and 2010 eruptions (Charbonnier and Gertisser, 2008; Lube et al., 2011; Gertisser et al., 2012; Charbonnier et al., 2013; Cronin et al., 2013), at Volcán de Colima (Mexico) in 1991, 1998-1999 and 2015 (Capra et al., 2016; Macorps et al., 2018; Reyes-Dávila et al., 2016; Sarocchi et al., 2011; Saucedo et al., 2002; Saucedo et al., 2004), at Soufriere Hills, Montserrat (Calder et al., 1999; Cole et al., 2002; Loughlin et al., 2002; Ogburn et al., 2014), and at Unzen, Japan (Fujii and Nakada, 1999; Miyabuchi, 1999).

The mode of emplacement of such long runout BAFs is often

interpreted as granular-fluid-based PDCs in the classification of Branney and Kokelaar (2002), characterized by density-stratified currents with a high-concentration granular dispersion (in which grain interactions dominate) at lowermost levels, from which the very poorly sorted, more massive deposits are emplaced; and more dilute, higher levels, in which ash is carried in turbulent gaseous suspension (Breard and Lube, 2017; Kelfoun, 2017). In the proximal and medial area, units of valleyconfined BAF deposits show lithofacies of massive deposits (mBLA) with moderate clast segregation, suggesting internal flow dynamics governed by high grain-dispersive pressure that induced segregation processes such as kinetic sieving (Middleton, 1970; Savage and Lun, 1988) and kinematic squeezing (Le Roux, 2003) of the largest clasts. In the distal areas, clast segregation becomes more subtle and discrete, which implies a progressive decrease in grain-dispersive pressure due to fewer grain interactions and therefore a decrease in kinetic energy produced inside the flow during transport. While channel confinement and sinuosity maintain high kinetic energy and momentum inside the most voluminous and mobile PDC events (units mBLA1 and mBLA2) through high-grain dispersive pressures and clast segregation processes, a sudden decrease in channel confinement when these two PDCs entered the Río Guacalate, at ~10 km from the summit, favored lateral spreading and thinning (due to mass conservation) of the currents, in which the decrease in particle collisions together with the increase in grain interlocking in the coarse-rich basal region resulted in the loss of kinetic energy and flow momentum. The lack of strong changes in the grain size distributions of the fine sub-populations inside the seven valley-confined BAF lobate front units (Figs. 7 and 8, Tables 1 and 2) imply that little segregation occurred and fragmentation of clasts was mostly driven by attrition where particles break from either impact, compression, frictional or shear forces (and combination of these), and perhaps auto brecciation (sudden pulverization of blocks into ash upon impact). The high content of fines (between 17 and 25 wt% for fractions ≥4 phi) inside the valley-confined BAF deposits (Fig. 7 and Table 2) imply the presence of a self-limiting attrition process, probably due to the lower frequency of impacts between coarse particles and the small contact stresses during these impacts which limit further breakage. By filling the void space between particles, fines could decrease the porosity of such long-runout BAFs and impact their interstitial gas pressure (and lower their effective friction coefficient) during transport. While the volume and mass flux of collapsed material from the head scarp of Las Lajas are the two most important parameters controlling the flow mobility and runout distances here, the high initial temperatures of both the solid fraction and gas due to the incorporation of fresh, hot and vesicular pyroclasts from the Sub-Plinian phase inside the most voluminous and mobile PDC events (units mBLA1 and mBLA2) could have also enhanced their runouts. Such a self-limiting attrition process was absent inside the two most proximal, short-runout distance PDCs (units mBLA6 and mBLA7), where the mean particle diameters and sorting within the coarse sub-populations vary significantly (Fig. 8 and Table 2).

The presence of sharp discontinuities in lithofacies, grain size and sorting at the interface between two valley-confined units, as well as the lack of ash-layers in between individual units (except between overbank units mBLA-OB1 - m(B)LA-OB2, see Fig. 6), can be explained by the mechanical erosion exerting by the shear of the basal portion of subsequent pulses as they travelled over previously deposited units. Our detailed stratigraphic work shows much evidence of stacked, massive flow units deposited by rapid stepwise aggradation of successive BAF pulses, similar to the June 14, 2006, Merapi BAFs (Charbonnier and Gertisser, 2011) and the 1991, 1999 and 2015 Colima BAFs (Macorps et al., 2018; Sarocchi et al., 2011; Saucedo et al., 2004). This model differs from the one proposed by Risica et al. (2022) who suggest the emplacement of a single, predominantly sustained and braided, but fluctuating, granular-fluid-based PDC over a 1.5-h duration. We did not find any field evidence to support such a sustained PDC behavior and interpret their claims as being made on less comprehensive stratigraphic work, with sampling and data collection being limited to the distal area, close to La Reunion golf resort and San Miguel de Los Lotes. Therefore, their facies interpretation and inferred, sustained PDC dynamics are limited to the two most distal PDC events that reached the Río Guacalate during the peak of PDC activity between 3.00 and 3.30 pm and corresponding to the emplacement of the two lowermost valley-confined and overbank units only (mBLA1-mBLA2 and mBLA-OB1 - m(B)LA-OB2 in Fig. 6).

The presence of a thin (~0.5-m-thick) stratified- to cross-stratified ash-cloud surge deposits that inundated large areas on the southeastern proximal flank (Fig. 3 and units sLA1, csLA2 in Figs. 5 and 6), is associated with numerous downed trees with a mean azimuth direction of $130 \pm 20^{\circ}$ from North (Fig. 3 inset), measured on both sides of the Las Lajas channel. This is consistent with the general NW-SE orientation of elongated topographic features of the southeastern flank (including the old collapse structure) and thus supports the interpretation that the June 3rd PDCs, including the dilute parts of the currents, were largely controlled by the topography from proximal to distal reaches (Fig. 4a). However, this interaction displays contrasting features in the landscape: proximal areas (≤ 4 km) that face the main direction of current have been heavily scoured, eroded and largely removed of any vegetation (Fig. 4d,g), while proximal areas in the lee of topographic barriers are characterized by bent trees that are still rooted and even trees that have not been delimbed, as well as only weakly eroded ground (i.e.,

interfluves between El Jute and Las Lajas barrancas, Fig. 4e). This suggests that topographic barriers and obstacles favored the development of vortices and eddies in the currents (i.e., Gardner et al., 2018; Guinn et al., 2022), which in turn triggered a thermal lofting and detachment of the pressure front, and the development of a singe zone, as seen for example in a large distal portion on the west bank of the western Las Lajas channel, upstream of San Miguel de Los Lotes (Fig. 3). During transport, the strong turbulence of the head region of the PDC led to entrainment of ambient air within the gas-particle mixture. This led to expansion of the head (waxing) and further contributes to fluidization of the mixture associated with trapped interstitial gases.

Field evidence suggests that each current was characterized by marked vertical gradients in velocity, turbulence, current density, maximum clast size, dynamic pressure, and temperature (Fig. 4h-k), and that these physical parameters constantly evolved in time and space within the current's transport and depositional system. Similar interpretations were made for the May 1980 Mount St Helens and 2010 Merapi PDCs(Charbonnier et al., 2013; Cronin et al., 2013; Guinn et al., 2022; Komorowski et al., 2013).

Finally, the most striking feature of the June 3rd PDCs was its ability to overspill the Las Lajas main channel at several locations (3 PDC overspill sites and 7 surge detachment sites, Fig. 3). Flow confinement in a narrow and sinuous channel enhances the mobility and runout of individual channelized BAF pulses. When these conditions occur, the progressive valley infilling from successive gravitational collapse events promotes the overspill and lateral spreading of the upper and marginal regions of the main flow body, generating highly mobile overbank flows that travel outside of the main valley. These processes occurred at Fuego during the peak PDC activity between 3.00 and 3.30 pm on June 3rd. A combination of 1) progressive infilling of the proximal and medial portions of the Las Lajas channel by PDCs emplaced during the sub-Plinian phase after 1.00 pm; 2) partial filling of the distal, eastern Las Lajas channel section by the first PDC that stopped just after the RN-14 bridge around 2.30 pm; 3) presence of a channel constriction and 90° bend at PDC overspill site 3, ~8.2 km from the summit (Fig. 3); 4) large, continuous headwall failures and rapid retrogressive collapses of a thick and large portion of the perched pyroclastic material accumulated in the old collapse structure (T2 in Fig. 12); all contributed to generate PDCs with the most voluminous and highest mass-fluxes of the June 3rd sequence (units mBLA1 and mBLA2).

A new field campaign in March 2022 allowed us to decipher the sequence of events that led to the major PDC overspill that buried twothirds of the village of San Miguel de Los Lotes and killed hundreds of people on that day. A fresh stratigraphic section inside the Las Lajas channel at PDC overspill site 3 (Fig. 13), exposing the entire distal June 3rd valley-confined BAF deposit sequence, as well as remnants of two pre-2018 valley-confined BAF terraces, reveals that the two first PDC pulses (units mBLA1 and mBLA2) that occurred between 3.05 pm and 3.12 pm (Fig. 2) and destroyed the RN-14 bridge did not overspill the channel at this location, but only filled it by ~60% of its capacity, as shown by their complete exposure in the channel and the presence of the top of unit mBLA2, located ~5 m below the top of the old channel western bank made of historical tephra fallout and PDC deposits (Fig. 13). It is only with the third PDC pulse, which arrived between 3.12 pm and 3.16 pm (Fig. 2), that the currents were finally able to spill over the western channel bank and flow toward San Miguel de Los Lotes. The basal portion of the deposits associated with this third PDC pulse can be seen inside the upper \sim 5 m of the channel section, on top of unit mBLA2, while the upper portion formed a \sim 3 m thick, wedge-shaped overbank deposit (unit mBLA-OB1), on top of the western channel bank (Fig. 13). The presence of surficial lobate fronts and overbank deposits on top of unit mBLA-OB1 (i.e., unit m(B)LA-OB2 in Figs. 5 and 6) just a few tens to hundreds of meters upstream of San Miguel de Los Lotes (Fig. 3), suggest that other PDC pulses were able to take the same direction and reach runout distances of 8-9 km after 3.18 pm, as witnessed by CONRED personnel located near El Rodeo village (Fig. 2E).



Fig. 13. Picture taken at overspill site 3 (see Fig. 3 for location) in March 2022 inside Las Lajas barranca showing exposed valley-confined (mBLA facies) and overbank PDC units from June 3rd, 2018, overtopping the remnants of two pre-2018 valley-confined BAF terraces and the old channel western bank made of historical tephra fallout and PDC deposits. The basal portion of the 2018 PDC deposits associated with the third PDC pulse can be seen inside the upper \sim 5 m of the channel section, on top of unit mBLA2, while the upper portion formed a \sim 3 m thick, wedge-shaped overbank deposit (unit mBLA-OB1), on top of the western channel bank.

3.3. Implications for future PDCs at Fuego

The impact of the June 3rd, 2018, eruption on exposed populations and infrastructures was the largest since the 1932 and 1974 eruptions, and this eruption remains the greatest in terms of human impact within Fuego's extended history (Naismith et al., 2019). Moreover, this eruption was of a different character from the 2015-2018 paroxysms: preceded by a greater period of quiescence, and possibly not preceded by lava effusion, the peak of eruption intensity was reached in just five hours and the peak of PDC activity occurred >1.5 h after the sub-Plinian phase, during a period when no significant eruptive event was recorded. Both ground-based observations and satellite detection agree on the presence of meteorological clouds throughout much of the June 3rd, 2018, eruption (Naismith et al., 2019), and while the volcano flanks were visible through the first hours of the eruption in the morning, video footages taken during the sub-Plinian phase at midday and peak of PDC activity in the afternoon show a high concentration of clouds and ash obscuring most of the volcanic edifice on that day. The two main eruptive events that led to the high death toll during this eruption were: 1) the generation of large, voluminous PDCs with high mass-fluxes from continuous headwall failures and rapid retrogressive collapses of a thick and large portion of the perched pyroclastic material accumulated in the old collapse structure of the SE flank; and 2) the rapid (~10 min.) infilling of the distal Las Lajas channel section by the first two PDCs in the afternoon that crossed the RN-14 bridge and led to major overspills at 8.2 km from the summit (overspill site 3 in Fig. 3), where both a channel constriction and 90° bend allowed the following PDC pulses to take the direction of San Miguel de Los Lotes.

The gradual infill of the old collapse structure in the upper SE flank of Fuego by eruptive deposits accumulated since 2015 has been documented by time series of both ground-based and satellite images (Albino et al., 2020; Dualeh et al., 2021; Risica et al., 2022). During our field campaign in March 2022, we could observe fresh pyroclastic material already filling the base of the 2018 collapse scarp, and with such the current frequency of paroxysms since 2015, pyroclastic accumulation in this area and associated gravitational collapses could certainly occur again. Such changes in pyroclastic accumulation on the upper slopes of Fuego should be monitored on a timely basis, using both ground-based and remote sensing tools. Once the pyroclastic material accumulated inside the collapse structure reaches a critical thickness and extent as determined by slope stability models, development of new hazard mitigation procedures should be put in place to anticipate the initiation

of a large gravitational collapse and the generation of large volume and long runout PDCs and their associated overbank flows. As an example, volume-, mass-flux- and distance-dependent critical channel capacities for the generation of overbank flows and detached surges can be developed using high resolution DEMs and numerical mass flow models to better estimate the inundation area of these hazardous unconfined PDCs from each potentially affected barranca surrounding Fuego (i.e., Charbonnier et al., 2020; Gueugneau et al., 2021; Ogburn et al., 2014; Ogburn and Calder, 2017). For this, timely acquisition of up-to-date DEMs of the barrancas immediately following each rainy season and/or major lahar event is crucial for an accurate assessment of the critical channel capacities and areas prone to such PDC overspill processes.

Following the 2018 eruption, major efforts have been made by the communities to recover quickly from the impact of the 2018 eruption on infrastructures: the section of the RN-14 road on the SE slopes of Fuego has been entirely renovated and the Las Lajas bridge was rebuilt with impact-proof material and raised by several meters to better resist to the more frequent lahar activity that has occurred in Las Lajas since the emplacement of the 2018 PDC deposits. Finally, the breach made by the 2018 PDCs on the western bank of the Las Lajas barranca at overspill site 3 (Fig. 3) was dammed and filled with sediments, and the 2018 pyroclastic material emplaced in the distal section of the eastern Las Lajas channel just upstream of the RN-14 road was excavated, all to prevent future flows to overspill and take the direction of San Miguel de Los Lotes. The channel base at overspill site 3 has been strongly deepened by lahar activity and is now >30 m below the top of the western bank. This should allow the next series of PDCs that reach this site to stay channelized in the main Las Lajas barranca and prevent them from directly overspilling in the direction of the village. Progressive infilling of the channel by small, successive lahar and PDC events could occur quickly, and continuous efforts should be made to minimize the potential of PDC overspill in this area by producing a series of hazard and risk assessments that could lead to timely evacuations of the various communities living on the volcano slopes ahead and during the early stages of the paroxysmal cycles.

4. Conclusions

The June 3rd, 2018, eruption of Fuego volcano was an unusually large paroxysmal eruption for Fuego with much longer-runout PDCs compared to previous paroxysmal activity, and its impact on exposed populations and infrastructures was the largest since the 1932 and 1974

eruptions. The combination of stratigraphic surveys, and sedimentological and textural analyses of the PDC deposits carried out just after the first rainy season after the eruption, allows us to discuss in some detail the processes that controlled PDC generation and emplacement during the 2018 eruption.

The PDC deposits comprise: (1) valley-confined PDC deposits in the Las Lajas, El Jute, Ceniza and Santa Teresa/Seca barrancas; (2) overbank PDC deposits, where parts of the channeled PDCs spread laterally onto interfluves at several sites along the main channels and were subsequently re-channeled into the surrounding river valleys and adjacent tributaries; and (3) thin (\sim 0.5-m-thick) ash-cloud surge deposits that inundated large areas on the proximal-medial flanks, especially along all seven main barrancas of the volcano.

The June 3rd PDC and tephra fallout deposits show strong relative abundance and textural variations, both between the different barrancas affected by the 2018 eruption (mainly Ceniza, Seca and Las Lajas), and within the different PDC units emplaced in Las Lajas on afternoon of June 3rd. The various lithological components recognized are tentatively grouped into three main categories (free crystals, juveniles and accidental lithics) and the degree of clast oxidization and hydrothermal alteration is thought to be correlated with the time the clast spent in contact with hot, humid atmospheric gases, i.e., the time it was stored inside the 2015 collapse structure containing 'perched' pyroclastic material on the proximal southeastern flank of Fuego.

Geophysical monitoring and recording of the PDC activity on June 3rd as carried out by INSIVUMEH and our results allow us to propose a conceptual model of PDC generation where a sequence of packages of material involved in discrete failure events (T1-T3) of a perched mass of pyroclastic material accumulated within an old collapse structure on the upper SE flank, corresponds to the emplacement of a series of pulses of valley-confined PDCs down the Las Lajas channel. In this model, headwall failures and gravitational collapses correlate with specific stratigraphic, sedimentological and textural characteristics of the valleyconfined PDC units. The duration of individual granular collapse events serves as a proxy for the mobility of the triggered series of PDCs. Evidence of stacked, massive flow units deposited by rapid stepwise aggradation of successive block-and-ash flow (BAF) pulses and their distribution along the southeastern flank supports the interpretation that the June 3rd PDCs, including the dilute parts of the currents, were largely controlled by the topography. The lack of strong changes in the grain size distributions of the fine sub-populations inside the seven valley-confined BAF lobate front units, together with their high content of fines, imply the presence of a self-limiting attrition process, decreasing the bulk porosity of such long-runout BAFs and lowering their effective friction coefficient during transport to reach longer runout distances.

Finally, the two main eruptive events responsible for the high death toll during this eruption were: 1) the generation of large, voluminous PDCs with high mass-fluxes from continuous headwall failures and rapid retrogressive collapses of a thick and large portion of the perched pyroclastic material accumulated in the old collapse structure of the SE flank; and 2) the rapid (\sim 10 min.) infilling of the distal Las Lajas channel section by the first two PDCs in the afternoon that crossed the RN-14 bridge and led to major overspills at 8.2 km from the summit (overspill site 3), where both a channel constriction and 90° bend allowed the subsequent PDC pulses to advance in the direction of San Miguel de Los Lotes. In the case of the June 2018 eruption, the PDC generation by partial collapse of previously and recently accumulated material at and around the summit made available the large volumes of material that were required to produce long runout flows that inundated Los Lotes. In particular, the progressive infilling and then subsequent overspills allowed for overbank flows to be directed toward the community of Los Lotes.

Author statement

Sylvain J. Charbonnier: Conceptualization, Methodology, Investigation, Writing, Visualization, Funding Acquisition.

Franco Garin: Investigation, Writing, Visualization.

Lizzette A. Rodríguez: Conceptualization, Methodology, Investigation, Visualization, Review and Editing, Funding Acquisition.

Karla Ayala, Sahira Cancel: Investigation, Visualization.

Rudiger Escobar-Wolf: Conceptualization, Methodology, Investigation, Review and Editing, Funding Acquisition.

Gustavo Chigna, Carla Chun-Quinillo, Dulce González: Conceptualization, Methodology, Investigation, Resources, Review and Editing.

William Chigna, Kevin Chun-Quinillo, Roberto Mérida, Francisco Juarez: Investigation, Resources, Review and Editing.

Eliza S. Calder: Conceptualization, Methodology, Review and Editing, Funding Acquisition.

Declaration of Competing Interest

The authors declare that they have no known competing financial interests or personal relationships that could have appeared to influence the work reported in this paper.

Data availability

Data will be made available on request.

Acknowledgements

This work was supported by the National Science Foundation (NSF) RAPID grant #1841852 to Charbonnier, Rodríguez and Escobar-Wolf, NSF CAREER grant #17511905 to Charbonnier as well as NE/T010517/1 (Ixchel: Building understanding of the physical, cultural and socio-economic drivers of risk for strengthening resilience in the Guatemalan cordillera) to Calder and Escobar-Wolf. Charbonnier and Rodríguez would like to thank all Guatemalan colleagues, as well as all students and postdoctoral fellows (Ana Jiménez, Valentin Gueugneau, Luke Varner, Jarelys González, Luke Bowman, Beth Bartel, Gustavo Béjar, Giovanni Nin, Paola Rivera, Pedro Salamanca, Quelyn Bekkering, Sanna Mairet, Evelyn Jobe, Brandi Pertryk) for their participation and help during the field campaigns and/or laboratory analyses. We also thanks D. Sarocchi, an anonymous reviewer and J.-L. Macías for their careful reviews of the manuscript.

References

Albino, F., Biggs, J., Escobar-Wolf, R., Naismith, A., Watson, M., Philips, J.C., Chigna Marroquin, G.A., 2020. Using TanDEM-X to measure pyroclastic flow source location, thickness, and volume: application to the 3 June 2018 eruption of Fuego volcano, Guatemala. J. Volcanol. Geotherm. Res. 406, 107063.

Andrews, B.J., 2014. Dispersal and air entrainment in unconfined dilute pyroclastic density currents. Bull. Volcanol. 76 (9), 852.

Andrews, B.J., Manga, M., 2011. Effects of topography on pyroclastic density current runout and formation of coignimbrites. Geology 39 (12), 1099–1102.

Andrews, B.J., Manga, M., 2012. Experimental study of turbulence, sedimentation, and coignimbrite mass partitioning in dilute pyroclastic density currents. J. Volcanol. Geotherm. Res. 225–226, 30–44.

Berlo, K., Stix, J., Roggensack, K., Ghaleb, B., 2012. A tale of two magmas, Fuego, Guatemala, Bull, Volcanol. 74 (2), 377–390.

Blott, S.J., Pye, K., 2001. GRADISTAT: a grain size distribution and statistics package for the analysis of unconsolidated sediments. Earth Surf. Process. Landf. 26, 1237–1248.

Borselli, L., Sarocchi, D., 2009. Deconvolution of mixtures of lognormal components inside particle size distributions (DECOLOG 6.0.1). http://www.decolog.org/.

Branney, M.J., Kokelaar, P., 2002. Pyroclastic Density Currents and the Sedimentation of Ignimbrites, vol. 27. Geological Society, p. 142.

Breard, E.C.P., Lube, G., 2017. Inside pyroclastic density currents—Uncovering the enigmatic flow structure and transport behavior in largescale experiments. Earth Planet. Sci. Lett. 458, 22–36.

Brosch, E., Lube, G., 2020. Spatiotemporal sediment transport and deposition processes in experimental dilute pyroclastic density currents. J. Volcanol. Geotherm. Res. 401, 106946.

- Brown, R.J., Andrews, G., 2015. Deposits of pyroclastic density currents. In: The Encyclopedia of Volcanoes, Second edition. Elsevier, pp. 631–648.
- Bursik, M.I., Woods, A.W., 1996. The dynamics and thermodynamics of large ash flows. Bull. Volcanol. 58, 175–193.
- Bustillos, J.A., Romero, J.E., Guevara, A.C., Díaz-Alvarado, J., 2018. Tephra fallout from the long-lasting Tungurahua eruptive cycle (1999-2014): variations through eruptive style transition and deposition processes. Andean Geol. 45 (1), 47–77.
- Calder, E.S., Cole, P.D., Dade, W.B., Druitt, T.H., Hoblitt, R.P., Huppert, H.E., Ritchie, L., Sparks, R.S.J., Young, S.R., 1999. Mobility of pyroclastic flows and surges at the Soufriere Hills Volcano, Montserrat. Geophys. Res. Lett. 26 (5), 537–540.
- Capra, L., Macías, J.L., Cortés, A., Dávila, N., Saucedo, R., Osorio-Ocampo, S., Arce, J.L., Gavilanes-Ruiz, J.C., Corona-Chávez, P., García-Sánchez, L., Sosa-Ceballos, G., 2016. Preliminary report on the July 10-11, 2015 eruption at Volcán de Colima: pyroclastic density currents with exceptional runouts and volume. J. Volcanol. Geotherm. Res. 310, 39-49.
- Charbonnier, S., Gertisser, R., 2008. Field observations and surface characteristics of pristine block-and-ash flow deposits from the 2006 eruption of Merapi Volcano, Java, Indonesia. J. Volcanol. Geotherm. Res. 177, 971–982.
- Charbonnier, S.J., Gertisser, R., 2011. Deposit architecture and dynamics of the 2006 block-and-ash flows of Merapi Volcano, Java, Indonesia. Sedimentology 58 (6), 1573–1612.
- Charbonnier, S.J., Germa, A., Connor, C.B., Gertisser, R., Preece, K., Komorowski, J.-C., Lavigne, F., Dixon, T., Connor, L., 2013. Evaluation of the impact of the 2010 pyroclastic density currents at Merapi volcano from high-resolution satellite imagery, field investigations and numerical simulations. J. Volcanol. Geotherm. Res. 261, 295–315.
- Charbonnier, S.J., Thouret, J.-C., Gueugneau, V., Constantinescu, R., 2020. New insights into the 2070calyrBP pyroclastic currents at El Misti Volcano (Peru) from field investigations, satellite imagery and probabilistic modeling. Front. Earth Sci. 8.
- Cole, P.D., Calder, E.S., Sparks, R.S.J., Clarke, A.B., Druitt, T.H., Young, S.R., Herd, R.A., Harford, C.L., Norton, G.E., 2002. Deposits from dome-collapse and fountaincollapse pyroclastic flows at Soufrière Hills Volcano, Montserrat. Geol. Soc. Lond. Mem. 21 (1), 231–262.
- Cronin, S.J., Lube, G., Dayudi, D.S., Sumarti, S., Subrandiyo, S., 2013. Insights into the October– November 2010 Gunung Merapi eruption (Central Java, Indonesia) from the stratigraphy, volume and characteristics of its pyroclastic deposits. J. Volcanol. Geotherm. Res. 261, 244–259.
- Doronzo, D.M., Valentine, G.A., Dellino, P., De Tullio, M.D., 2010. Numerical analysis of the effect of topography on deposition from dilute pyroclastic density currents. Earth Planet. Sci. Lett. 300 (1–2). 164–173.
- Druitt, T.H., 1998. Pyroclastic density currents. In: Gilbert, J.S., Sparks, R.S.J. (Eds.), The Physics of Explosive Volcanic Eruptions, vol. 145. Geological Society, London, Special Publications, pp. 145–182.
- Dualeh, E.W., Ebmeier, S.K., Wright, T.J., Albino, F., Naismith, A., Biggs, J., Ordonez, P. A., Boogher, R.M., Roca, A., 2021. Analyzing explosive volcanic deposits from satellite-based radar backscatter, Volcán de Fuego, 2018. J. Geophys. Res. Solid Earth 126 e2021JB022250.
- Escobar Wolf, R.P., 2013. Volcanic Processes and Human Exposure as Elements to Build a Risk Model for Volcan de Fuego, Guatemala (PhD thesis).. Michigan Technological University, 216 pp.
- Ferres, D., Escobar Wolf, R., 2018. Informe Tecnico: Volcan de Fuego. Technical Report. Cooperacion Espanola. URL. http://bibliotecadigital.aecid.es/bibliodig/i18n/consulta/registro.cmd?id=8751.
- Fujii, T., Nakada, S., 1999. The 15 September 1991 pyroclastic flows at Unzen Volcano (Japan): a flow model for associated ash-cloud surges. J. Volcanol. Geotherm. Res. 89 159–172
- Gardner, J.E., Nazworth, C., Helper, M.A., Andrews, B.J., 2018. Inferring the nature of pyroclastic density currents from tree damage: the 18 May 1980 blast surge of Mount St. Helens, USA. Geology 46, 795–798.
- Gertisser, R., Cassidy, N.J., Charbonnier, S.J., Nuzzo, L., Preece, K., 2012. Overbank blockand- ash flow deposits and the impact of valley-derived, unconfined flows on populated areas at Merapi volcano, Java, Indonesia. Nat. Hazards 60 (2), 623–648. https://doi.org/10.1007/s11069-011-0044-x.
- Global Volcanism Program, 2022. In: Venzke, E. (Ed.), [Fuego (342090)] in Volcanoes of the World, v. 4.8.2. Smithsonian Institution. Retrieved from. https://volcano.si.edu/volcano.cfm?vn=342090.
- Grunewald, U., Sparks, R.S.J., Kearns, S., Komorowski, J.C., 2000. Friction marks on blocks from pyroclastic flows at the Soufriere Hills volcano, Montserrat: implications for flow mechanisms. Geology 28, 827–830.
- Gueugneau, V., Charbonnier, S., Esposti Ongaro, T., De'michieli Vitturi, M., Peruzzetto, M., Mangeney, A., Bouchut, F., Patra, A.K., Kelfoun, K., 2021. Synthetic benchmarking of concentrated pyroclastic current models. Bull. Volcanol. 83 (11), 1–32.
- Guinn, N.K., Gardner, J.E., Helper, M.A., 2022. Dynamic pressure evolution within the 18 May 1980 Mount St. Helens pyroclastic density current: evidence from tree damage. Bull. Volcanol. 84, 38.
- Heiken, G., Wohletz, K., 1985. Volcanic Ash: Berkeley. University of California Press, U. S., p. 246
- INSIVUMEH, 2018a. Descenso de Flujos Piroclásticos, vol. 36. Bolentín Vulcanólogico Especial, Volcán de Fuego.
- INSIVUMEH, 2018b. Descento de Flujos Piroclásticos Hacia La Barranca Seca, vol. 59. Bolentín Vulcanólogico Especial, Volcán de Fuego.
- INSIVUMEH, 2018c. Erupcion con Flujoc Piroclásticos, vol. 27. Bolentín Vulcanólogico Especial, Volcán de Fuego.
- INSIVUMEH, 2018d. Finaliza la erupcion, vol. 33. Bolentín Vulcanólogico Especial, Volcán de Fuego.

- INSIVUMEH, 2018e. Flujos Piroclásticos Barranca Las Lajas, vol. 44. Bolentín Vulcanólogico Especial, Volcán de Fuego.
- INSIVUMEH, 2018f. Flujos Piroclásticos Barranca Las Lajas, vol. 47. Bolentín Vulcanólogico Especial, Volcán de Fuego.
- INSIVUMEH, 2018g. Flujos Piroclásticos Barranca Las Lajas Y Jute, vol. 38. Bolentín Vulcanólogico Especial, Volcán de Fuego.
- Jessop, D.E., Kelfoun, K., Labazuy, P., Mangeney, A., Roche, O., Tillier, J.-L., Trouillet, M., Thibault, M., 2012. LiDAR derived morphology of the 1993 Lascar pyroclastic flow deposits, and implication for flow dynamics and rheology. J. Volcanol. Geotherm. Res. 245–246, 81–97.
- Kelfoun, K., 2017. A two-layer depth averaged model for both the dilute and the concentrated parts of pyroclastic currents. J. Geophys. Res. Solid Earth 122 (6), 4293-4311
- Komorowski, J.C., Jenkins, S., Baxter, P.J., Picquout, A., Lavigne, F., Charbonnier, S.J., Gertisser, R., Preece, K., Cholik, N., Budi-Santoso, A., 2013. Paroxysmal dome explosion during the Merapi 2010 eruption: processes and facies relationships of associated high-energy pyroclastic density currents. J. Volcanol. Geotherm. Res. 261, 260–294
- Kubo Hutchison, A., Dufek, J., 2021. Generation of overspill pyroclastic density currents in sinuous channels. J. Geophys. Res. Solid Earth 126 (10), 1–20.
- Le Roux, J.P., 2003. Can dispersive pressure cause inverse grading in grain flows? Discuss. J. Sedim. Res. 73, 333–334.
- Lerner, G.A., Jenkins, S.F., Charbonnier, S.J., Komorowski, J.C., Baxter, P.J., 2022. The hazards of unconfined pyroclastic density currents: a new synthesis and classification according to their deposits, dynamics, and thermal and impact characteristics. J. Volcanol. Geotherm. Res. 421, 107429.
- Loughlin, S.C., Calder, E.S., Clarke, A., Cole, P.D., Luckett, R., Mangan, M.T., Pyle, D.M., Sparks, R.S.J., Voight, B., Watts, R.B., 2002. Pyroclastic flows and surges generated by the 25 June 1997 dome collapse, Soufrière Hills Volcano, Montserrat. In: Druitt, T.H., Kokelaar, B.P. (Eds.), The Eruption of Soufrière Hills Volcano, Montserrat, from 1995 to 1999, Geological Society of London's Memoirs, vol. 21, pp. 191–210.
- Lube, G., Cronin, S.J., Thouret, J.C., 2011. Kinematic characteristics of pyroclastic density currents at Merapi and controls of their avulsion from natural and engineered channels. Geol. Soc. Am. Bull. 123, 1127–1140.
- Lube, G., Breard, E.C.P., Esposti-Ongaro, T., Dufek, J., Brand, B., 2020. Multiphase flow behaviour and hazard prediction of pyroclastic density currents. Nat. Rev. Earth Environ. 1 (7), 348–365.
- Lyons, J.J., Waite, G.P., Rose, W.I., Chigna, G., 2010. Patterns in open vent, strombolian behavior at Fuego volcano, Guatemala, 2005–2007. Bull. Volcanol. 72 (1), 1.
- Macorps, E., Charbonnier, S.J., Varley, N.R., Capra, L., Atlas, Z., Cabré, J., 2018. Stratigraphy, sedimentology and inferred flow dynamics from the July 2015 block-and-ash flow deposits at Volcán de Colima, Mexico. J. Volcanol. Geotherm. Res. 349, 99–116.
- Martin, D.P., Rose Jr., W.I., 1981. Behavioral patterns of Fuego volcano, Guatemala. J. Volcanol. Geotherm. Res. 10 (1–3), 67–81.
- Martínez-Martínez, J., Mediato, J.F., Mata, J.F., Ordóñez, B., del Moral, B., Bellido, E., Pérez-López, R., Rodríguez-Pascua, M.A., Vegas, J., Lozano Otero, G., Mateos, R.M., Sánchez, N., Galindo, I., 2023. Early fumarolic minerals from the Tajogaite volcanic eruption (La Palma, 2021). J. Volcanol. Geotherm. Res. 435, 107771 https://doi.org/10.1016/j.jvolgeores.2023.107771.
- Middleton, G.V., 1970. Experimental studies related to problems of flysch sedimentation. In: Lajoie, J. (Ed.), Flysch Sedimentology in North America. 7. Geol. Soc. Can. Spec. Paper, pp. 253–272.
- Miyabuchi, Y., 1999. Deposits associated with the 1990–1995 eruption of Unzen volcano, Japan. J. Volcanol. Geotherm. Res. 89, 139–158.
- Naismith, A.K., Watson, I.M., Escobar-Wolf, R., Chigna, G., Thomas, H., Coppola, D., Chun, C., 2019. Eruption frequency patterns through time for the current (1999–2018) activity cycle at Volcán de Fuego derived from remote sensing data: evidence for an accelerating cycle of explosive paroxysms and potential implications of eruptive activity. J. Volcanol. Geotherm. Res. 371, 206–219.
- Ogburn, S.E., Calder, E.S., 2017. The relative effectiveness of empirical and physical models for simulating the dense undercurrent of pyroclastic flows under different emplacement conditions. Front. Earth Sci. 5, 1–26.
- Ogburn, S.E., Calder, E.S., Cole, P.D., Stinton, A.J., 2014. Chapter 10 the effect of topography on ash-cloud surge generation and propagation. Geol. Soc. Lond. Mem. 39, 179–194.
- Pardini, F., Queier, M., Naismith, A., Watson, I.M., Clarisse, L., Burton, M.R., 2019. Initial constraints on triggering mechanisms of the eruption of Fuego volcano (Guatemala) from 3 June 2018 using IASI satellite data. J. Volcanol. Geotherm. Res. 376, 54–61.
- Patrick, M.R., Harris, A.J., Ripepe, M., Dehn, J., Rothery, D.A., Calvari, S., 2007. Strombolian explosive styles and source condition: insights from thermal (FLIR) video. Bull. Volcanol. 69 (7), 769–784.
- Reyes-Dávila, G.A., Arámbula-Mendoza, R., Espinasa-Pereña, R., Pankhurst, M.J., Navarro-Ochoa, C., Savov, I., Vargas-Bracamontes, D.M., Cortés-Cortés, A., Gutiérrez-Martínez, C., Valdés-González, C., Domínguez-Reyes, T., González-Amezcua, M., Martínez-Fierros, A., Ramírez-Vázquez, C.A., Cárdenas-González, L., Castañeda-Bastida, E., Vázquez Espinoza del los Monteros, D.M., Nieto-Torres, A., Campion, R., Courtois, L., Lee, P.D., 2016. Volcán de Colima dome collapse of July, 2015 and associated pyroclastic density currents. J. Volcanol. Geotherm. Res. 320, 100–106.
- Risica, G., Rosi, M., Pistolesi, M., Speranza, F., Branney, M.J., 2022. Deposit-derived block-and-ash flows: the hazard posed by perched temporary tephra accumulations on volcanoes; 2018 Fuego disaster, Guatemala. J. Geophys. Res. Solid Earth 127 e2021JB023699.

- Rose, W.I., Self, S., Murrow, P.J., Bonadonna, C., Durant, A.J., Ernst, G.G.J., 2008. Nature and significance of small volume fall deposits at composite volcances: insights from the October 14, 1974 Fuego eruption, Guatemala. Bull. Volcanol. 70 (9) 1043–1067
- Sarocchi, D., Sulpizio, R., Macías, J.L., Saucedo, R., 2011. The 17 July 1999 block-and-ash flow (BAF) at Colima Volcano: new insights on volcanic granular flows from textural analysis. J. Volcanol. Geotherm. Res. 204 (1), 40–56.
- Saucedo, R., Macías, J.L., Bursik, M.I., Mora, J.C., Gavilanes, A., Cortes, A., 2002. Emplacement of pyroclastic flows during the 1998–1999 eruption of Volcan de Colima, Mexico. J. Volcanol. Geotherm. Res. 117, 129–153.
- Saucedo, R., Macías, J.L., Bursik, M., 2004. Pyroclastic flow deposits of the 1991 eruption of Volcán de Colima, Mexico. Bull. Volcanol. 66 (4), 291–306.
- Savage, S.B., Lun, C.K.K., 1988. Particle size segregation in inclined chute flow of dry cohesionless granular solids. J. Fluid Mech. 189, 311–335.
- Schwarzkopf, L.M., Schmincke, H.-U., Troll, V.R., 2001. Pseudotachylite on impact marks of block surfaces in block-and-ash flows at Merapi volcano, Central Java, Indonesia: Internat. J. Earth Sci. 90, 769–775.
- Schwarzkopf, L.M., Schmincke, H.-U., Troll, V.R., 2002. Friction marks on blocks from pyroclastic flows at the Soufriere Hills volcano, Montserrat: implications for flow mechanisms: comment. Geology 30, 190.

- Schwarzkopf, L.M., Schmincke, H.-U., Cronin, S.J., 2005. A conceptual model for blockand- ash flow basal avalanche transport and deposition, based on deposit architecture of 1998 and 1994 Merapi flows. J. Volcanol. Geotherm. Res. 139, 117–134.
- Ui, T., Matsuwo, N., Sumita, M., Fujinawa, A., 1999. Generation of block and ash flows during the 1990–1995 eruption of Unzen volcano, Japan. J. Volcanol. Geotherm. Res. 89, 123–137.
- Valentine, G.A., 1987. Stratified flow in pyroclastic surges. Bull. Volcanol. 49 (4), 616 630.
- Valentine, G.A., 2020. Initiation of dilute and concentrated pyroclastic currents from collapsing mixtures and origin of their proximal deposits. Bull. Volcanol. 82 (2), 20.
- Waite, G.P., Nadeau, P.A., Lyons, J.J., 2013. Variability in eruption style and associated very long period events at Fuego volcano, Guatemala. J. Geophys. Res. Solid Earth 118 (4), 1526–1533.
- Walker, G.P.L., 1983. Ignimbrite types and ignimbrite problems. J. Volcanol. Geotherm. Res. 17, 65–88.
- Woods, A.W., Bursik, M.I., Kurbatov, A.V., 1998. The interaction of ash flows with ridges. Bull. Volcanol. 60, 38–51.
- Yamamoto, T., Takada, A., IshizukaMiyaji, Y.N., Tajima, Y., 2005. Basaltic pyroclastic flows of Fuji volcano, Japan: characteristics of the deposits and their origin. Bull. Volcanol. 67, 622.